Introduction to Photoacoustic Spectroscopy with Step Scan and Constant Velocity Scan FTIR Spectrometers

J. F. McClelland*, S. J. Bajic, R. W. Jones, and L. M. Seaverson*

Ames Laboratory, Iowa State University
Ames, IA 50011 USA
and
***MTEC Photoacoustics, Inc.**
P.O. Box 1095, Ames, IA 50014 USA
515/292-7974 (voice), 515/292-7125 (fax)
e-mail: mtec@mtecpas.com
www.mtecpas.com

July, 1996

This is a preprint of a chapter to appear in
Modern Techniques of Applied Molecular Spectroscopy
edited by Dr. Francis M. Mirabella Jr.
and published by John Wiley & Sons, Inc.

TABLE OF CONTENTS

1.0 Introduction

1.1 Rationale for Use

Photoacoustic spectroscopy (PAS) measures a sample's absorbance spectrum directly with a controllable sampling depth and with little or no sample preparation. This rapid direct analysis capability is applicable to nearly all samples encompassing a wide range of absorbance strengths and physical forms. Other key features of PAS include: non-destructive; non-contact; applicable to macrosamples and microsamples; insensitive to surface morphology; spectral range from the UV to far-infrared; operable in photoacoustic absorbance, diffuse reflectance, and transmission modes; capable of measuring spectra of all types of solids (sheet, chunk, pellet, powder, semi-solid) without exposure to air or moisture; and also applicable to liquids and gases. This high level of versatility provided by PAS is the primary reason that it is used in industrial and other research laboratories.

1.2 History and Basic Idea of PAS

Alexander Graham Bell discovered PAS in 1880 while he was investigating possible means for optical communications [1] as shown in Figure 1.1. Bell observed that a beam of light focused on a sample produced an audible sound in the air around the sample if the beam was turned on and off at an acoustic frequency. He also found that strongly absorbing samples produced a louder sound or photoacoustic signal than weakly absorbing materials. The photoacoustic signal variation with sample absorbance was recognized by Bell as a way to measure absorbance spectra of materials, and he was able to demonstrate a primitive form of PAS. His spectroscopic apparatus appears in Figure 1.2. Practical exploitation of Bell's discovery was not initially achievable because further advances were needed in photoacoustic signal generation theory, in photoacoustic detector and spectrometer instrumentation, and in photoacoustic methods for specific analyses.

Since the 1980's, PAS has become a valuable analytical technique due to developments such as the Fourier Transform Infrared (FTIR) Spectrometer, low noise electronics, high sensitivity microphones, computerized data handling and methods for specific analyses. Research and development continues in all the areas mentioned. For example, new capabilities of instrumentation such as step-scan FTIR are enabling spectroscopists to use PAS to obtain results not previously possible. This chapter will discuss new advances since publication of the authors' last chapter on the subject entitled "A Practical Guide to FTIR Photoacoustic Spectroscopy" [2].

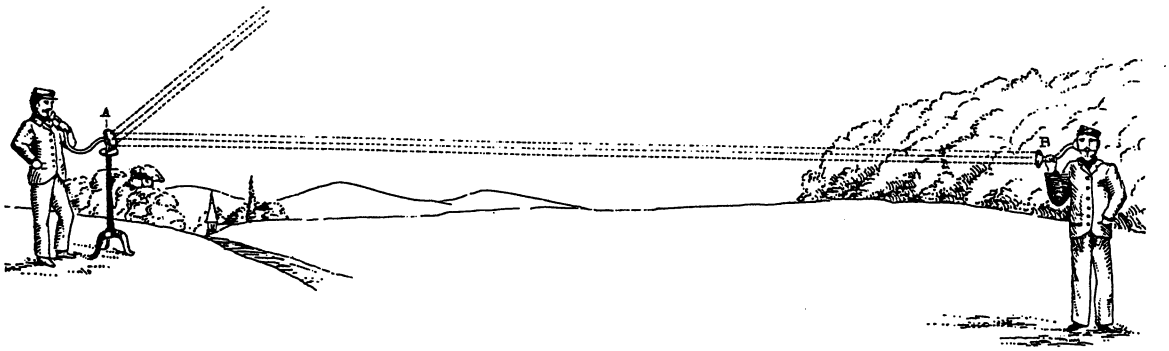

Figure 1.1 This figure from an 1881 publication [1] of A.G. Bell shows a voice message being communicated by intensity modulated sunlight utilizing his recently discovered photoacoustic effect.

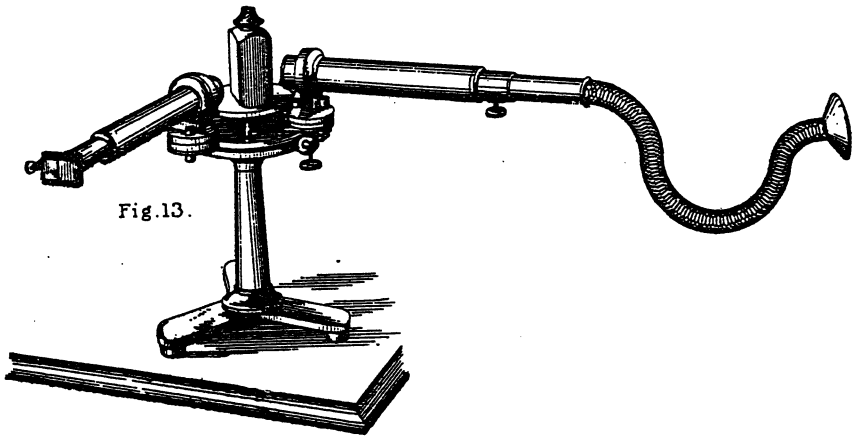

Figure 1.2 Bell recognized the possibility of using the photoacoustic effect in spectroscopic applications and developed a prism spectrometer including a hearing tube to facilitate listening to the photoacoustic signal response form various samples. Reproduced from [1].

1.3 Controllable Sampling Depth

The controllable sampling-depth feature of PAS is a result of the photoacoustic signal generation process, which involves absorption of light in the sample and production of heat followed by propagation of heat-generated thermal waves to the sample surface. Heat is then transferred into the adjacent gas, changing its pressure, which is sensed by a microphone as the photoacoustic signal. As the thermal waves propagate from the region where absorption occurred to the sample's light-irradiated surface, they decay rapidly, much like light does as it propagates through an absorbing medium. This decay process limits the depth beneath the sample surface from which signal generation occurs. Thus there is a mechanism for controlling sampling depth. Thermal waves have a decay coefficient that is proportional to the square root of the frequency at which the light is modulated. Consequently, the sampling depth, L, is decreased when the modulation frequency, f, is increased. The sampling depth is given by:

$$L = (D/\pi f)^{1/2} \tag{1.1}$$

where D is the sample's thermal diffusivity [3]. The sampling depth in photoacoustic measurements is usually stated to be the length, L, although due to the decay process there is not a sharp cut-off at a depth of L. For typical polymer materials where D is approximately 10^{-3} cm^2/s, L can be varied in FTIR photoacoustic measurements from a few micrometers to 100 or so micrometers by adjusting the frequency, f.

Information regarding the depth at which light is absorbed in a sample can also be gained from the phase shift between the intensity modulation of the light beam that is incident on the sample and the photoacoustic signal response. The phase shift between excitation and response is due to the finite time required for thermal waves to propagate from the site within the sample where absorption occurs to the surface of the sample where heat is transferred to the detector's gas atmosphere where gas expansion and pressurization results.

1.4 Practical Uses of Controllable Sampling Depth

The controllable sampling-depth of PAS is the key feature of the technique and has a number of uses:

1.) It allows spectra of totally opaque samples to be measured without the usual thinning or dilution common to transmission and diffuse reflectance spectroscopies. In PAS the effective sample thickness or optical path length for a sample is not determined by physical thickness but rather by the sampling depth given by Equation 1.1. It can be adjusted to an appropriate value for the absorbance values to be measured by properly setting the modulation frequency produced by the FTIR spectrometer. Thus the laborious and error prone task of reproducible sample thinning or dilution required for quantitative analyses in transmission and diffuse reflectance spectroscopies is replaced by simply setting an FTIR mirror velocity parameter for most PAS analyses.

2.) It facilitates analysis of layered samples or samples with concentration gradients. Both the magnitude and the phase of the photoacoustic signal can provide depth-distribution information. Signal magnitudes change with modulation frequency, in

part because of the change in sampling depth given by Equation 1.1. The magnitudes of bands from components having different depth distributions will therefore change with modulation frequency differently, so the comparison of spectra taken at various frequencies can provide qualitative depth distributions.

The phase shift approach is especially useful in determining the ordering and thickness of layered polymer materials. With this approach the ordering sequence of layers is determined by the relative phase shifts of specific absorbance bands associated with the different layers. Bands with larger phase shifts are assigned to deeper layers. The thickness of a layer on top of a substrate can be determined from the amount of phase shift caused to substrate bands due to the finite transit time for thermal-waves transiting across the layer.

The various uses of controlled sampling depth and its limiting factors will be discussed in more detail in the theory and applications sections of the chapter.

2.0 Signal Generation Theory and Data Analysis Treatments

2.1 Signal Generation Model - Introduction

Photoacoustic signal generation theory has been based on various models since the discovery of PAS by Bell. The modern theory uses a model with elements from the works of Parker [4], Rosenscwaig and Gersho [3], and McDonald and Wetsel [5]. A one dimensional model is shown in Figure 2.1 with the light beam of average intensity, I_0, assumed to oscillate in intensity at a modulation frequency, f, and to be incident normal to the sample's surface. After a reflection loss, RI_0, at the sample's surface, the light beam intensity decays exponentially as it propagates into the sample at a rate according to the sample's optical absorption coefficient, α. Heat is produced proportional to the amount of light absorption occurring in each layer of the sample. This process results in each light absorbing layer of the sample oscillating in temperature at the frequency, f, and becoming a source for thermal waves that propagate in the one-dimensional model back toward the light-irradiated surface of the sample. The thermal waves decay during propagation with a decay coefficient,

$$a_s=(\pi f/D)^{1/2}, \qquad (2.1)$$

where D is the sample's thermal diffusivity [3]. Thermal waves from layers within one decay length given by $1/a_s=L$ of the irradiated sample surface are responsible for transferring most of the heat into the gas and for thermal expansion driven photoacoustic signal generation. L is usually stated to be the sampling depth of a photoacoustic measurement as described in the introduction, although some signal contribution comes from as deep as $2\pi L$.

When a thermal wave reaches the sample/gas interface, a small fraction of the thermal wave crosses the interface and causes a temperature oscillation in the gas, which generates the photoacoustic signal in the form of a gas pressure fluctuation. Unfortunately, a large fraction of the thermal wave is reflected back into the sample at the interface. Most samples are physically much thicker than L, and the reflected thermal wave decays to zero within the sample. The thermal-wave reflection loss is an unfortunate fact of the physics of PAS signal generation and is a costly loss in terms of the signal-to-noise ratio of PAS measurements. Consequently, PAS detectors and spectrometers must be designed with care in order to optimize performance and to produce a signal-to-noise ratio that is acceptable relative to other sampling techniques. On the other hand, if the sample is much thinner than L, as with microsamples, the signal is enhanced by multiple thermal energy transfers as the thermal wave reflects back and forth from various faces of the sample.

2.2 Photoacoustic Signal Magnitude

The schematic diagram of Figure 2.1 shows the one dimensional signal generation model, where L is the nominal sampling depth [3, 5]. As the beam penetrates the sample, its intensity decays exponentially, with a decay length equal to the reciprocal of the optical absorption coefficient, α. If α increases, the signal magnitude increases because a larger

fraction of the beam energy is deposited within a distance L of the sample surface. When $1/\alpha >> L$ (as for α_1 in Figure 2.1), the signal increases linearly with α, as shown by the *Thermal Only* line in Figure 2.2. As $1/\alpha$ approaches L, the linear relation is lost (onset of saturation) because most of the beam energy is now absorbed within depth L. Eventually, as for α_2 in Figure 2.1, $1/\alpha << L$ and full saturation is achieved. The signal no longer increases after full saturation with increasing α because virtually all of the beam is absorbed well within L. Beyond the full saturation point, only the sample reflectivity, R, which is related to α, affects the signal magnitude, because the reflectivity affects the fraction of the incident beam that actually enters the sample.

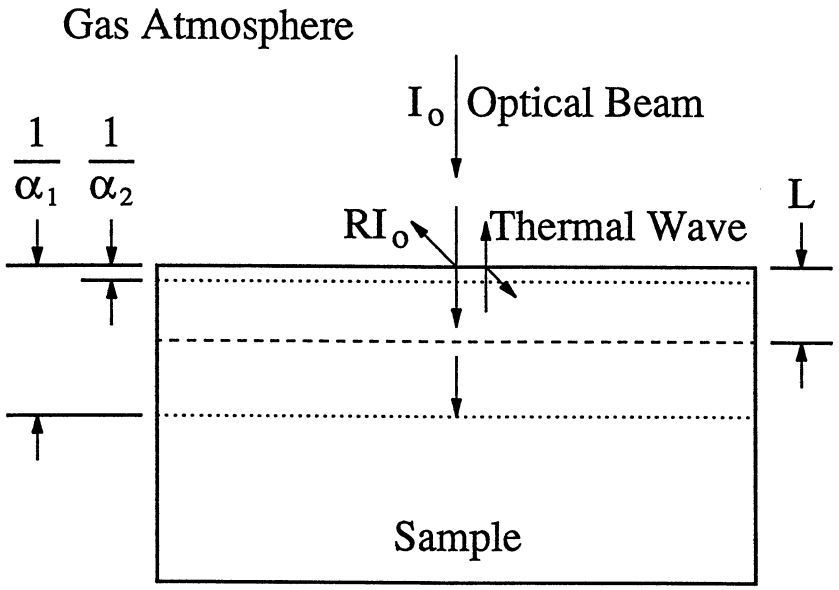

Figure 2.1 One-dimensional model schematic of photoacoustic signal generation as discussed in the text.

Another signal generation mechanism, quite different from thermal waves, is observable from mid-range to low values of α. In this instance, the photoacoustic signal has a thermal wave component, as discussed above, and a small acoustic component due to thermal expansion and contraction of the sample itself, excited by the temperature oscillations within the sample [5]. This acoustic contribution causes a small increase as shown in Figure 2.2 in the thermally driven gas signal in the mid to low range of α, which is negligible at higher α.

Figure 2.2 also shows a third contribution from a background signal which is sometimes observed as α decreases. This contribution is due to scattered light being absorbed by the walls of the sample chamber within the photoacoustic detector. The background contribution shown is estimated from typical experimental data.

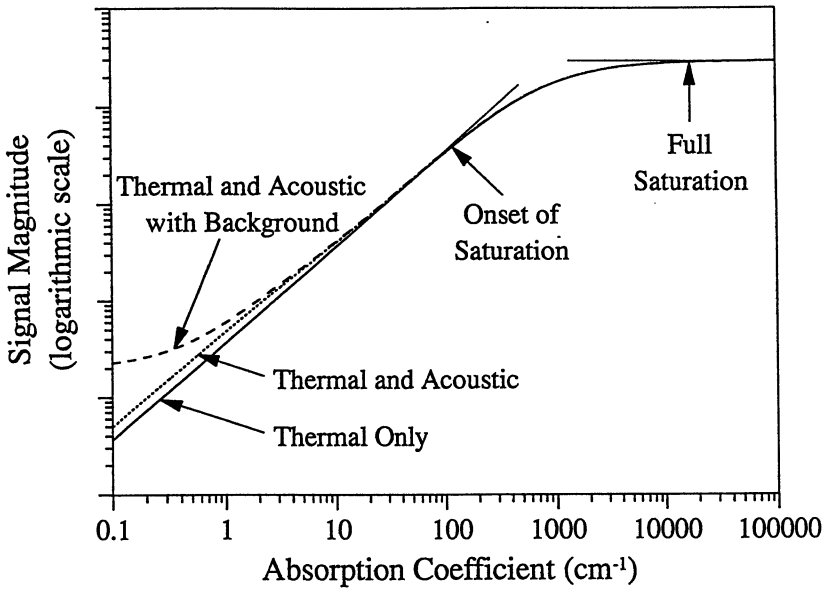

Figure 2.2 Photoacoustic signal magnitude versus absorption coefficient as calculated from models based on thermal, and thermal and acoustic signal generation mechanisms with D(sample) = 10^{-3}cm^2/s, f = 100Hz, sample thermal expansion coefficient = $3 \cdot 10^{-4}$/K, D(helium) = 2.8 cm^2/s, sample thickness = 3 mm, sample thermal conductivity = $1.7 \cdot 10^{-3}$W/cmK. The background contribution was estimated from experimental data and added to the thermal and acoustic curve because this contribution would be difficult to calculate from first principles.

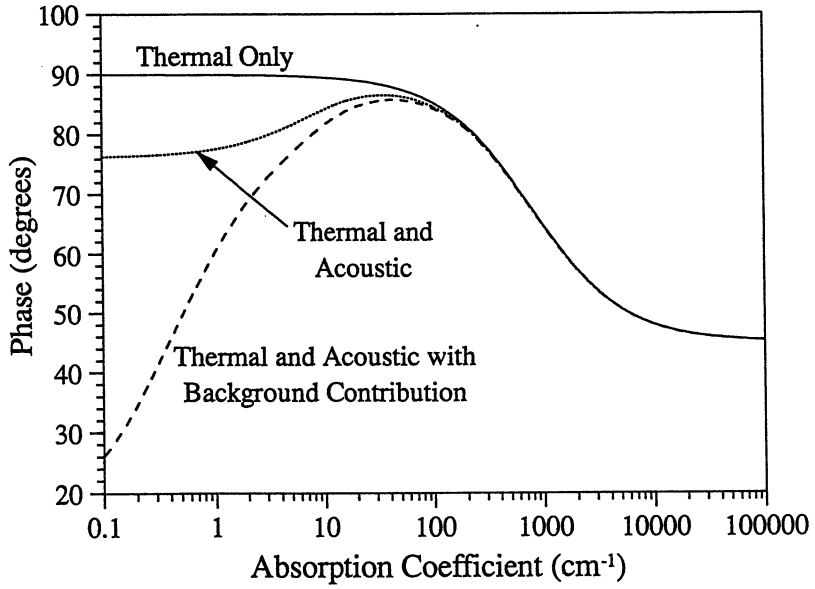

Figure 2.3 Photoacoustic signal phase versus absorption coefficient as calculated from thermal, and thermal and acoustic signal generation models using the same parameter values as in Figure 2.2. The background contribution was estimated from experimental data due to the impracticality of calculating it from first principles.

2.3 Photoacoustic Signal Phase

The discussion of signal generation so far has focused on the behavior of the magnitude of the photoacoustic signal. The signal's phase also has valuable information. The phase of a photoacoustic signal is defined as the phase difference between the modulation of the incident light beam absorbed by the sample and the photoacoustic signal response. For a thermally and optically homogeneous sample the phase is predicted to approach a value of 45^{o} at high values of α and 90^{o} at low values of α provided that the sample is thick relative to L and that the thermal model is used without the acoustic and background signal contributions [3]. This phase behavior is shown as the *Thermal Only* line in Figure 2.3, which also shows the phase dependence when the acoustic and background signal contributions are included, both of which cause smaller phase shifts or faster signal evolution than the thermal model alone in regions of low α. The phase of the background signal is estimated from typical experimental data. The background contribution produces a smaller phase shift or faster signal response than otherwise expected. This signal behavior can be explained, as in the magnitude case, by scattered light generating a signal at the interior walls of the photoacoustic detector, which are usually anodized aluminum comprising a layered material (thin lower thermal conductivity layer on a higher thermal conductivity substrate). This type of sample is not homogeneous as assumed in the signal generation model results plotted without background contribution in Figure 2.3. Theoretical calculations [6] and the authors' experimental results show that a layered signal generator of the type described can produce signals with phase shifts smaller than 45^{o} whereas bare metal such as stainless steel produces a background signal at 45^{o} in agreement with the homogeneous sample model.

2.4 Photoacoustic Signal Saturation

As shown in Figure 2.2, the photoacoustic signal ceases to increase with absorption at high values of α and therefore, the PAS signal may saturate, as concentrations of analytes in a sample increase, depending on an analyte's absorption coefficient. In nearly all PAS analysis applications, however, full saturation does not occur. Measurements are made in the linear range before the onset of saturation and the nonlinear range after onset. Consequently, the strong absorbance bands in PAS spectra are truncated relative to the weak bands due to saturation. Thus, weak bands appear more prominently in plots of PAS spectra as a result of the nonlinearity of PAS spectra relative to transmission spectra where saturation is not present due to thinning or dilution. Figure 2.4 shows typical PAS magnitude signal behavior versus α for several different modulation frequencies. These curves are calculated from the thermal model [3]. Note that the onset and full saturation points move to higher α as the modulation frequency is increased. This frequency dependence implies that saturation of strong bands will be less in high modulation frequency spectra than in low, as is expected since the sampling depth, L, decreases with frequency.

The signal magnitudes shown in Figure 2.4 decrease with frequency as $1/f^{3/2}$ before onset of saturation and as $1/f$ after full saturation. The decrease in signal magnitude with f reduces the signal-to-noise ratio of PAS spectra if f is increased to reduce saturation and

equal signal averaging times are used. Thus there is a trade-off situation between signal-to-noise ratio and reduction of spectral saturation to be addressed in both quantitative and qualitative analysis applications. In quantitative PAS applications, factor analysis treatment of spectra by either Principal Components Regression (PCR) or Partial Least Squares (PLS) is usually able to accommodate considerable spectral nonlinearity while still producing Standard Errors of Prediction (SEP) less than 1%. Therefore, the higher signal-to-noise ratio and more rapid spectral acquisition of lower frequency PAS measurements are the trade-off choice. This is also usually the choice for qualitative analyses with computer searching, because the presence of nonlinearity does not strongly influence peak positions and most search software can perform searches based only on peak positions.

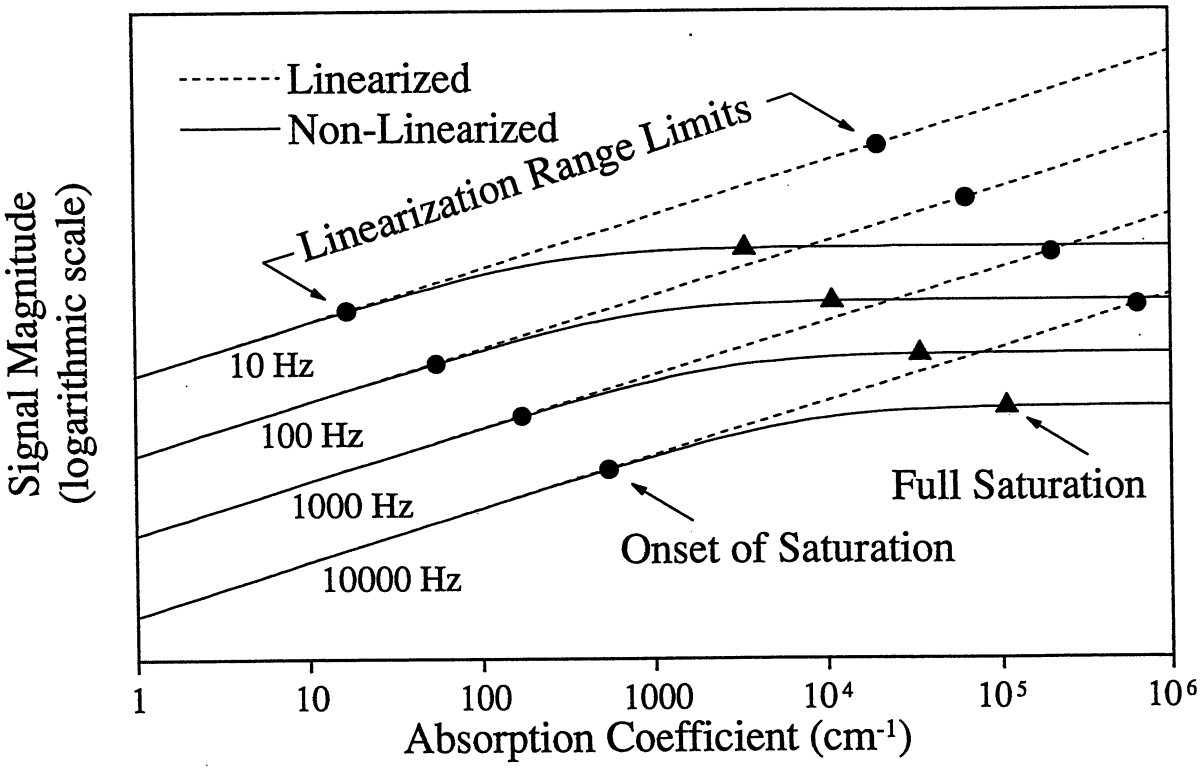

Figure 2.4 Photoacoustic signal behavior for different modulation frequencies as a function of sample absorption coefficient. Onset and full saturation points are shown as well as linearization extensions discussed in the text. The curves were calculated using $D = 10^{-3}$ cm^2/s.

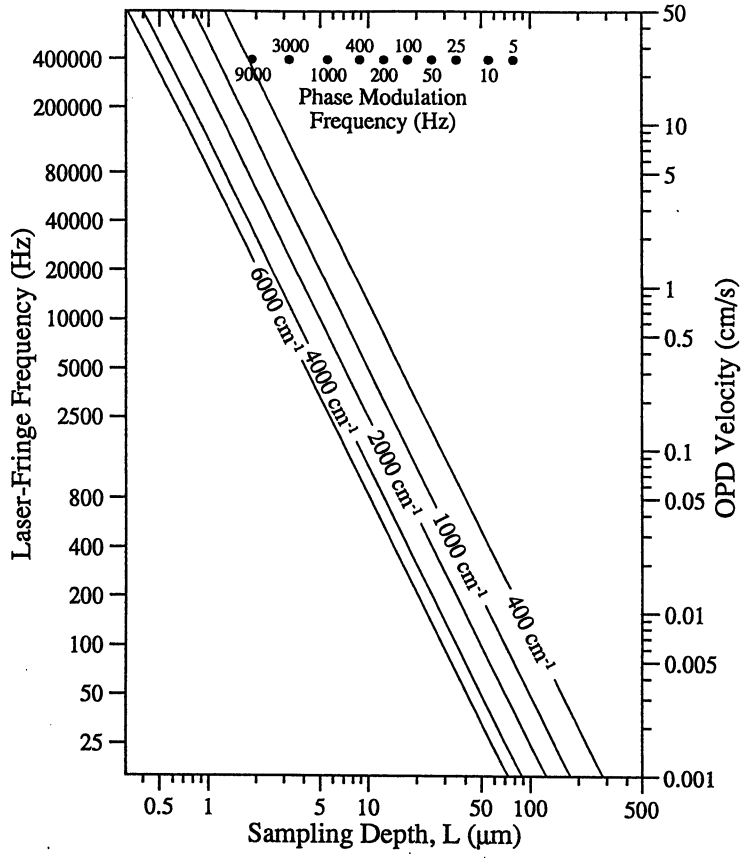

Figure 2.5 Sampling depth dependence on FTIR mirror velocity given in terms of optical path difference (OPD) velocity and helium-neon laser fringe frequency. A thermal diffusion coefficient, D, of $1x10^{-3}$ cm^2/s, typical of many polymers, is assumed. An increase in D would cause deeper sampling and vice versa.

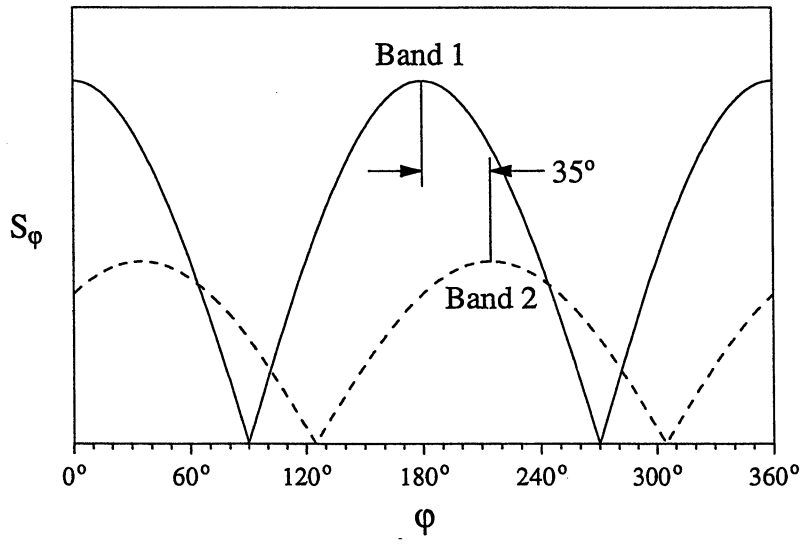

Figure 2.6 Variation of the peak magnitude of two absorbance bands as a function of phase angle. The origin of the phase angle axis is arbitrary.

2.5 Sampling Depth

PAS measurements over a range of modulation frequencies, including high frequencies, are important when samples with depth varying compositions are analyzed. Figure 2.5 shows the variation in sampling depth, L, as a function of FTIR spectrometer optical path difference (OPD) velocity and phase modulation frequency and the spectrum wavenumber for samples with a thermal diffusivity, $D = 10^{-3}$ cm^2/s, which is typical of many polymers. The diagonal lines in the plot each have a wavenumber label because an FTIR spectrometer, operating in constant velocity mode, modulates each wavenumber across the spectrum at a different frequency which depends on the mirror velocity of the spectrometer's interferometer according to the formula,

$$f = V\nu, \qquad (2.2)$$

where V is the optical path difference (OPD) velocity of the interferometer mirror and ν is the wavenumber. The mirror velocity is usually expressed either as the OPD velocity (right-hand vertical axis of Figure 2.5) or as the helium-neon laser-fringe frequency (left-hand vertical axis of Figure 2.5) which is the modulation frequency occurring at the laser wavelength of 632.8 nm corresponding to a laser wavenumber of 15,800 cm^{-1}.

When L is used to estimate sampling depth, it is important to note that this is valid only if there is adequate penetration of light to the depth L to generate a photoacoustic signal. If the optical decay length, $1/\alpha$, is shorter than L at a particular wavenumber in a spectrum, then the sampling depth is determined optically and the signal will have substantial saturation at that wavenumber. Due to the exponential decay of both light waves and thermal waves, the information obtained at a particular sampling depth is always skewed toward the sample surface.

The very deep sampling depths indicated in the lower right hand corner of Figure 2.5 are achieved only for α values in the 10 cm^{-1} and below range. Due to the low α values common to near-infrared spectra relative to the mid-infrared region, the near-infrared region often will offer the best opportunity for very deep sampling.

Very shallow sampling also presents some special considerations because PAS signal generation becomes weaker at high frequency, the acoustic response of the typical photoacoustic detector falls off above approximately 16 kilohertz, and FTIR interferometers have mirror velocity limits. In view of these limitations, it is important to note that it is possible to compute spectra using magnitude and phase data that have an effective sampling depth approximately a factor of 3 shallower than calculated from the actual modulation frequency. Consequently, the vertical axes of Figure 2.5 are extended above the 80 kilohertz and 5 cm/s OPD velocity points, which approximately mark the instrumental limit, to indicate the range extended by calculation. The computed spectra are called linearized spectra because the shallower effective sampling depth results in linear signal dependence on α for α values above the onset of saturation as shown in Figure 2.4. The linearization process involves synchronizing the interferograms of the sample and a surface absorber such as glassy carbon. The interferograms are transformed

using the surface absorber as a phase guide and the real and imaginary components are saved. The linearized spectrum, S_l, is calculated from:

$$S_l = (S^2_R + S^2_I)/1.414(S_I R_R - S_R R_I) \qquad (2.3)$$

where the subscripts R and I denote the real and imaginary parts of the sample (S) and reference (R) spectra [7]. The linearization calculation is based on the thermal signal generation model. The linearization calculation recently has been incorporated into the standard software of one FTIR manufacturer (Win-IR Pro, BioRad Inc.) and may be available from other FTIR firms in the future.

Phase modulation frequency points are shown at the top of Figure 2.5. Phase modulation is generated by operating the FTIR in a step-scan mode and oscillating the position of one of the interferometer mirrors at an amplitude corresponding to some number of helium-neon laser wavelengths. In this way, an intensity modulation is imposed on all wavenumbers of the infrared spectrum at the same phase modulation frequency, so only one value of L applies to all wavenumbers. If the waveform of the mirror oscillation is a square wave rather than sinusoidal, measurable photoacoustic signals are also generated at higher odd harmonics, such as the 3rd and the 9th, of the fundamental modulation frequency, which are shown in Figure 2.5 for a one kilohertz fundamental. State-of-the-art digital signal processing makes it possible to simultaneously measure the magnitude and phase of photoacoustic signals at the fundamental and the odd harmonics of the phase modulation frequency. Thus, spectra are obtained, for instance, with three different sampling depths simultaneously.

2.6 Interpretation of Photoacoustic Signal Phase Data

If the waveforms of the infrared beam's intensity modulation and of the photoacoustic signal excited by that beam are plotted together one observes that the photoacoustic response lags the excitation in time. This time lag between the two waveforms is due to the finite time for thermal waves to propagate first from where light is absorbed in the sample to its irradiated surface and then into the gas adjacent to the sample surface.

The time lag of the photoacoustic signal can also be viewed as a phase angle shift between the excitation and response waveforms. The phase shift due to propagation only in the gas is always 45^o as can be seen for very large values of α in Figure 2.3. When α is very large all of the incident beam is absorbed right at the irradiated surface and thermal wave propagation within the sample is negligible. Note that for the phase to be 45^o it is also necessary that the sample thickness be at least half the maximum distance that a thermal wave can travel in one modulation cycle. Otherwise, the phase is shifted by thermal waves reflecting off the back face of the sample and then propagating back to the irradiated surface. It is also necessary that the back face be thermally in contact with a backing material so that signal generation occurs only at the irradiated front surface of the sample.

As the sample's absorption coefficient decreases from high values to low, light is absorbed at increasingly deeper depths within the sample. Figure 2.3 shows the increasing phase shift for an optically and thermally homogeneous sample as α decreases to the low absorption range where the acoustic and scattered light background signal contributions become evident.

Layered polymer samples present a case where the sample is often highly inhomogeneous optically but usually fairly homogeneous thermally. A simple example is a thin coating on a thick substrate. If the substrate has a strong absorbance band where the coating is transparent, then absorbance by that band results in thermal waves being generated very close to the interface between the coating and the substrate. A phase shift is caused by the finite transit time for the thermal wave to propagate across the coating and into the gas. The phase shift, θ_t, can be calculated for thermal-wave propagation across a coating of thickness, t, from the thermal-wave velocity,

$$V = (4\pi Df)^{1/2}, \qquad (2.4)$$

as given in the classic text by Carslaw and Jaeger [8]. If T is the oscillation period ($T = 1/f$), then the product $VT = 2\pi L$ is the distance that a thermal wave travels in one cycle or 360°. This result is obtained by the substitution $L = (D/\pi f)^{1/2}$ (Equation 1.1). The phase shift, θ_t, is then given by

$$\theta_t = (t/2\pi L)\ 360^{\circ} \qquad \text{in degrees} \qquad (2.5)$$

or

$$\theta_t = t/L \qquad \text{in radians.} \qquad (2.6)$$

The propagation distance of a thermal wave per unit angle of phase shift is:

$$t/\theta_t = 2\pi L/360^{\circ} \qquad \text{in degrees} \qquad (2.7)$$

or

$$t/\theta_t = L \qquad \text{in radians.} \qquad (2.8)$$

Table 2.1 shows the ratio of propagation distance to angle for a range of modulation frequencies using a value of $D = 10^{-3}\text{cm}^2/\text{s}$ which is typical of polymers. The table also includes for comparison the corresponding values for the sampling depth L and for $VT = 2\pi L$ which is the distance a thermal wave can travel in one modulation cycle.

Table 2.1 Thermal wave propagation parameters for different modulation frequencies with $D = 10^{-3}$ cm²/s.

f(Hz)	*L*(μm)	*VT*(μm)	t/θ_t(μm/degree)
1	178	1120	3.1
10	56.4	354	0.98
50	25.2	159	0.44
100	17.8	112	0.31
400	8.92	56.0	0.16
1000	5.64	35.4	0.10
10000	1.78	11.2	0.031

Table 2.1 indicates that very small changes in depth cause degree-sized changes in phase with increasing sensitivity at higher frequencies. It is advantageous to make step-scan, phase-modulation measurements which readily yield phase information when using photoacoustic spectroscopy to study layered samples. This approach also results in constant modulation frequency across the entire spectrum rather than a linear frequency variation with wavenumber as in continuous scan measurements.

In a typical phase-modulation measurement orthogonal interferograms are measured simultaneously at the phase modulation frequency. More advanced FTIR systems with digital signal processing (DSP) capability and square-wave phase modulation are also able to simultaneously acquire data at the odd harmonic frequencies of the fundamental modulation frequency. The higher frequency data provides higher depth/degree resolution near the sample surface as indicated in Table 2.1.

A major interest in phase-modulation measurements is the relative phase shift differences between different absorbance bands in a sample's absorbance spectrum. As discussed earlier, the larger phase shifts are associated with absorption occurring deeper in the sample.

The phase shifts associated with different absorbance bands are best observed by plotting the amplitudes of absorbance peaks versus phase angle. Such plots are generated by measuring in-phase (I_0) and quadrature (I_{90}) interferograms simultaneously and calculating the interferogram I_φ at detection angle φ from:

$$I_\varphi = I_0 \cos\varphi + I_{90} \sin\varphi \qquad (2.9)$$

Equation 2.9 is Fourier transformed to get the spectrum S_φ at a specific detection angle φ. Repeating this process for different values of φ allows a plot to be made of S_φ versus φ.

S_φ is plotted versus φ for typical strong and weak absorbance bands in Figure 2.6. The plot shows a 35 degree phase shift between the strong (band 1) and weak (band 2) bands. Figure 2.6 could also represent a substrate band before (band 1) and after (band 2) a transparent coating is applied to the substrate. In this case the coating thickness, t, which produces a phase shift, θ_t, can be calculated from the expression:

$$t = 2\pi L\theta_t/360^\circ \qquad (2.10)$$

For a 35 degree phase shift, Equation 2.10 predicts a thickness of 10.9 μm using a thermal diffusivity of 10^{-3} cm^2/s and modulation frequency of 100 Hz to calculate the $L = (D/\pi f)^{1/2}$ term.

In many practical measurements the coating is not completely transparent at the peak wavenumber position of the substrate band being used to measure coating thickness versus phase shift. This results in a smaller phase shift being measured than would be the case if the coating were completely transparent. The smaller shift is due to the signal contribution from the coating which involves a shorter thermal wave propagation distance.

The reduced phase shift can be corrected for by a calculation based on the fact that the measured magnitude and phase are the vector sum of the signals generated in the coating and substrate [9]. In order to determine coating thickness it is necessary to obtain the phase shift, θ_S, for the substrate contribution alone. This can be done from the law of cosines formulas of trigonometry:

$$S_S = (S_T^2 + S_C^2 - 2S_TS_C\cos(\theta_T - \theta_C))^{1/2} \qquad (2.11)$$

and

$$\theta_S = \theta_T + \cos^{-1}((S_T^2 + S_S^2 - S_C^2)/2S_TS_S) \qquad (2.12)$$

where S_S, S_T, and S_C are the magnitudes of substrate, total, and coating spectra at the peak position of the substrate band used in the analysis. S_T and S_C and the corresponding phases θ_T and θ_C are measured from the spectra of the coated sample and a thick slab of the coating material. The two spectra are scaled so that the closest coating band to the substrate band is of equal magnitude prior to measuring S_T and S_C. S_S is calculated from equation 2.11 and then θ_S is calculated from 2.12. An example of this method is given in the Applications Section.

3.0 Instrumentation

3.1 Photoacoustic Detector

3.1.1 Detector Description

3.1.1.1 Availability. Photoacoustic detectors for FTIR spectrometers are available from the major FTIR spectrometer firms and FTIR accessory companies throughout the world and directly from the sole detector manufacturer* as of this writing. The MTEC model 300 photoacoustic detector is the instrument currently being manufactured and will be discussed in this section. An earlier book chapter [2] treated the MTEC model 200, the predecessor of the model 300. The model 300 is pictured in Figure 3.1.

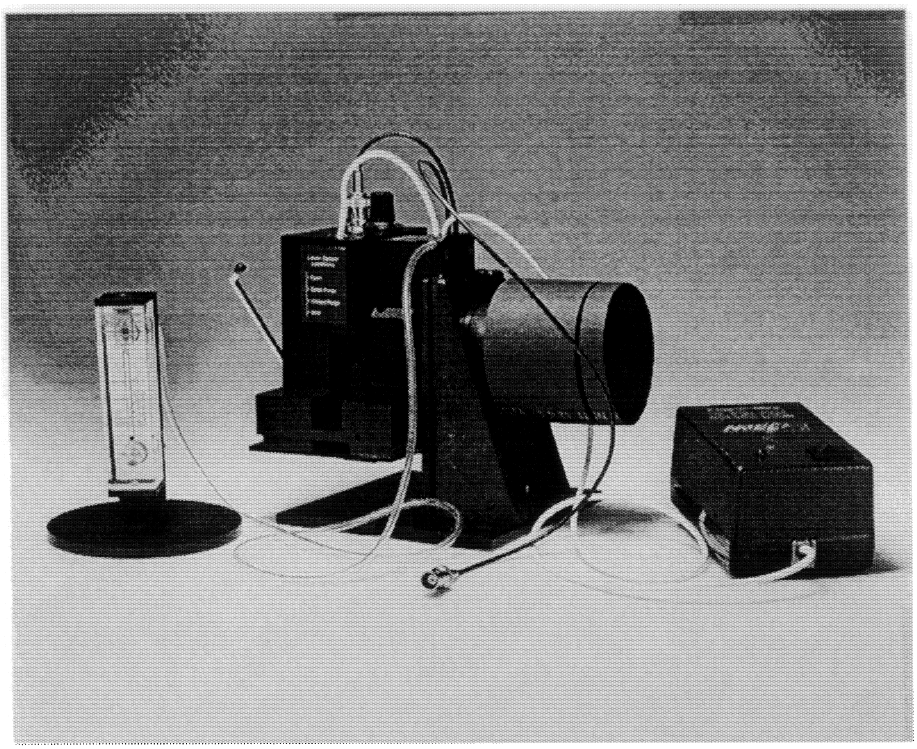

Figure 3.1 Photograph of the Model 300 MTEC photoacoustic detector mounted in a typical FTIR slide mount fixture (Nicolet Instruments). The helium flowmeter and desktop power supply are shown with their connections to the detector. The black cable with the BNC connector carries the detector signal to the FTIR. The rear control lever is visible between the flowmeter and detector. The black cylinder adjacent to the power supply is the purge coupler for the infrared beam path.

---

* MTEC Photoacoustics, Inc., PO Box 1095, Ames, Iowa 50014, USA;
Fax: 1-515-292-7125

3.1.1.2 Design. The model 300 is designed primarily for FTIR analysis of solid samples but can also be used for liquids and gases. The prefocused unit mounts in the FTIR sample slide fixture common to all FTIR spectrometers. A single lever controls the opening and closing (sealing) of the sample chamber and the flow of helium purge gas through the sample chamber. The photoacoustic signal pre-amplifier gains are controlled with a twelve step switch on the detector which is powered by a desk top power supply that operates on 115V (60Hz) or 230V (50Hz) line voltages.

3.1.1.3 Spectral Range. The spectral range of a photoacoustic detector depends on the transmission range of its window (See Table 3.1) and on the availability of suitable modulation frequencies for the spectral range of interest. Because the modulation frequency of a spectrometer beam is proportional to its wavenumber, as given by Equation 2.2, FTIR mirror velocities that are appropriate for the mid infrared can lead to modulation frequencies that are too high at shorter wavelengths. At 50,000 cm^{-1} in the ultraviolet, a practical modulation frequency of 316 Hz occurs at a mirror velocity of 100 Hz on the helium-neon laser fringe. In the near infrared the combination of the wavenumber and low absorption coefficients leads also to a need for low velocities such as 100 Hz. These considerations are summarized in Section 3.2.2.1.

In step-scan with phase modulation, the modulation frequency and amplitude are important. In this instance, the modulation frequency remains constant across all wavenumbers but the efficiency of modulation is variable with wavenumber depending primarily on the modulation amplitude as discussed in Section 3.2.2.2.

Table 3.1 Transmission ranges of commonly used photoacoustic detector window materials.

Material	Transmission Range
KBr *	40,000 cm^{-1} - 385 cm^{-1}
Quartz (UV grade)	54,000 cm^{-1} - 3700 cm^{-1}
CsI	33,000 cm^{-1} - 200 cm^{-1}
ZnSe	10,000 cm^{-1} - 515 cm^{-1}
Polyethylene	625 cm^{-1} - 10 cm^{-1}

* KBr is the standard window material used in the MTEC model 300 detector.

3.1.1.4 Detector Optics. The optics of the photoacoustic detector collect the light from the focal point at the FTIR's slide mount fixture and refocus the light downward into the detector's sample cup. A single 2X off-axis ellipsoidal mirror performs this function producing approximately a 5 mm diameter focal spot about 1.5 mm below the detector window in the sample cup.

The model 300 is prefocused and usually requires no optical adjustment when it is placed in the FTIR slide mount fixture. A liquid crystal infrared imaging disk is supplied by

MTEC to visualize the position of the infrared beam focal spot in the sample cup and guide lateral and vertical adjustments, if necessary, to center the beam.

3.1.2 Detector Installation

3.1.2.1 Mounting. The photoacoustic detector is positioned in the sample compartment of the FTIR by sliding it into the slide mount fixture common to all FTIR instruments as shown in Figure 3.1. The slide mount fixture should be located in the focal plane of the FTIR and centered on the beam axis.

3.1.2.2 Electrical connections. Electric power (±15VDC) for the detector's preamplifier is provided by a desk top power supply (115V/230V) with a switch to select the appropriate line voltage. Some FTIR spectrometers power the detector via a connector in the sample compartment making the desk top power supply unnecessary.

The photoacoustic detector signal is connected to the input of the FTIR electronics via a cable and connector specific for each instrument.

3.1.2.3 Purge Connection for Sample Chamber. Helium gas of zero grade (99.995%, total hydrocarbons < 0.5 ppm) or better should be used for purging the detector sample chamber. Purge rates from 5 cc/s to 20 cc/s are typical. There should be no valve between the gas cylinder pressure regulator valve and the detector's flow meter so that pressures only high enough to sustain the desired flow rate are used. Consequently, flow rate is to be controlled by the pressure regulator valve alone. This precaution reduces the chance of exposing the detector inadvertently to pressure surges. To further protect the detector it is advisable to turn the gas on and off and to adjust pressure only when the detector's rear lever is in the "seal" position. In this position gas bypasses the sample chamber and the microphone cannot be damaged by pressure surges.

3.1.2.4 Purged Optical Path. It is advantageous to maintain a water vapor and CO_2 free atmosphere not only in the FTIR but also in the optical path leading to the detector. Water vapor and CO_2 produce interfering absorbance bands and water vapor can damage moisture-sensitive optical components. The model 300 can be coupled directly to most FTIRs by a purge coupling tube as shown in Figure 3.1. Use of the purge coupling allows samples to be changed rapidly without having to wait for the FTIR sample compartment to be purged. The sample compartment door is normally left open at all times when the purge coupling is used. The purge coupling can also be used in sealed and desiccated FTIR spectrometers if it is connected to a dry air source.

3.1.3 Detector Operation

3.1.3.1 Sample Handling. The main sample cup of MTEC detectors accommodates samples up to 10 mm in diameter and 6 mm in thickness. Normally, sample specimens are considerably smaller. If samples are not already in the form of small specimens, they can be cut, punched, or abraded to obtain small specimens using a razor blade, scissors, hacksaw, cork borer (#6 and smaller), bench punch or abrasives. Samples are usually placed in stainless steel inner cups which fit concentrically into the main cup.

Different inner cup sizes are used with combinations of spacers to displace surplus gas volume in the main cup in order to enhance the signal, which is inversely proportional to the gas volume. There should, however, be an empty gas volume between the top of the sample and the main cup rim for generation of the photoacoustic signal. Usually the top of the sample should be approximately 1 mm to 2 mm below the main cup rim. This positioning is a reasonable compromise between signal generation efficiency and the main cup dimensions. Additional sample handling information is given in "A Practical Guide to FTIR Photoacoustic Spectroscopy" [2].

3.1.3.2 Control of H_2O and CO_2 Evolution from Samples. H_2O and CO_2 often evolve from the sample into the helium gas atmosphere of the sample chamber. Such vapors and gases produce absorbance bands in the spectra which can cause spectral interferences. There are several methods to reduce this problem. Samples can be predried in an oven or under a heat lamp prior to analysis. Very small amounts of powders can be put in the sample cup to lower the amount of contamination that would evolve from a full cup. Desiccants, such as magnesium perchlorate or molecular sieve spheres, can be placed in a second inner cup which is placed beneath the inner sample cup. Finally, the sample chamber purge time can be increased to dry the sample.

3.1.3.3 Detector Sample Chamber Purging. The detector is purged with helium to increase the signal magnitude by two to three times compared to air and to remove water vapor and CO_2 gas from the sample chamber. Dry, clean helium gas should be used with a "zero grade" rating or better. When the photoacoustic detector is in use, the flow rate is usually set between 5 cm/s and 20 cm/s and left at that setting throughout the analysis run for the sake of reproducibility and convenience. The detector purge valve is controlled by the rear lever that also controls the opening and closing of the sample chamber. The lever has four positions: open, open purge, sealed purge, and seal. When the lever is in the "open purge" position, helium gas flows over the sample. When the lever is in the "sealed purge" position, gas flows past but not over the sample. Fine powders can be blown out of the sample cup when the lever is in the "open purge" position. Therefore, it is recommended that the plastic tubing carrying the helium gas to the detector be momentarily finger pinched closed as the lever is moved between the open and "sealed purge" positions when fine powders are being measured. Other samples do not require this precaution.

Many samples may be loaded without any pause for purging when the detector is sealed. If the sample has moisture associated with it, a pause for purging may be necessary.

In quantitative measurements it may be important to perform purging in a reproducible manner. Reproducibility can be checked by acquiring several spectra with a particular gas flow rate and purge time and then overlaying the spectra to compare them.

It is important to leave the detector's rear lever in the seal position when the helium tank is first turned on and the gas line leading to the detector is being purged prior to purging the

detector itself. In the seal position, the sample chamber is by-passed and the microphone is protected from inadvertent pressurization due to an excessively high gas flow rate.

3.1.3.4 Spectrum Normalization. It is usually desirable to ratio the sample spectrum with the spectrum of a black absorber to remove spectral variations due to the source, optics, and detector responses. Carbon black powder has traditionally been used for this purpose, but it is a difficult substance to handle and is easily blown out of the sample cup. Consequently, a special carbon black coated membrane reference sample is supplied with MTEC detectors which remains permanently in a dedicated sample holder. This reference eliminates the need to handle carbon black powder and generates a very strong signal due to its low thermal mass.

At very low modulation frequencies the MTEC reference is unsuitable because the high signal level and low frequency cause vibration of the membrane. Therefore, a carbon black powder, glassy carbon, graphite, or 60% carbon-black-filled rubber sample should be used.

Photoacoustic spectra have arbitrary units in that the gain settings used when sample and reference spectra are measured will influence the scale of ordinate axis units. The thermal response of the sample, reference, and cell atmosphere also introduce an ordinate scale factor. As long as gain settings and thermal responses are kept consistent, the arbitrary nature of photoacoustic units does not interfere with quantitative analyses.

When very strongly absorbing samples such as a rubber tire are being analyzed, it is not uncommon to find that the baseline is not flat and must be corrected via the FTIR software. If a series of measurements are being done, for instance on tire rubber as a function of thermal/oxidation exposure, spectrum normalization can be done as follows. Single beam sample spectra are acquired and copied. The copied spectrum is very strongly smoothed to remove most of the sharp spectral peaks while leaving the broad spectral envelope unchanged. This smoothed spectrum is then used as the reference spectrum for normalization. The resulting normalized spectrum will have a very flat baseline and somewhat derivatized spectral band shapes. Spectra of this type can be subtracted with no scaling. In this way, very small spectral changes can be observed in the spectra of strongly absorbing materials. One caution is that prior to spectral subtraction sharp features due to the optics or gas contamination may be present in the normalized spectra. Such features are removed when subtractions are done if their source remains fixed during analyses.

3.1.3.5 Gain Switch Setting. It is important that the detector gain switch be consistently set when sample and reference spectra are collected. Otherwise scale changes will be present in spectra. Initially, settings should be determined by checking the magnitude of the interferogram to see that it is of a reasonable level for a given spectrometer. Usually several tenths to several volts peak-to-peak is suitable. Signal levels may be lower at high modulation frequencies.

3.1.3.6 System Checks. The optical alignment of the detector should be checked using the MTEC liquid crystal infrared imager.

A 100% line signal-to-noise test should produce a peak-to-peak noise of less than 0.2% at 2000 cm^{-1} ($\pm 50 cm^{-1}$) for the conditions in Table 3.2.

Table 3.2 Test parameters for measuring the FTIR-PAS system noise

Mirror velocity (OPD) = 0.1 cm/s
Resolution = 8 cm^{-1}
Source aperture = maximum
Spectral Range = 400 - 4000 cm^{-1}
Number of scans = 8
Apodization = Medium Beer-Norton
Sample = MTEC carbon black reference
Detector gas atmosphere = helium

Some FTIR systems will not allow exact duplication of the settings given in Table 3.2 and the closest available should be used. If the FTIR does not meet the noise level test, the beam splitter alignment should be checked using the FTIR's detector and the FTIR's mirror velocity control servo loop electronics should be tested.

3.1.3.7 Specialized Sampling Options. The MTEC model 300 and earlier MTEC detectors can be used with special options for diffuse reflectance (DRIFTS) and transmittance sampling (SH003) or for microsampling (SH004) [2]. Option SH003 allows the spectroscopist to switch between PAS, DRIFTS, and transmittance sampling by changing sampling heads on the standard sample holder. This is a useful option because the three sampling methods often produce complimentary data and can be used from the ultraviolet though the mid-infrared spectral regions. In other instances, SH003 allows the spectroscopist to rapidly determine which sampling method works best for a given sample.

Option SH004 allows measurement of single particle or fiber spectra without pressing to thin samples as is commonly done with infrared microscopes. Fibers with diameters as small as 10 μm and particles with diameters of 50 μm have been measured with SH004. Significantly higher sensitivity is possible by replacing the current 2X mirror with one of higher magnification.

3.2 FTIR Spectrometer

The performance level and the utility of PAS measurements are strongly influenced by the performance quality of the FTIR and the FTIR operating parameter selections available.

3.2.1 FTIR Operating Parameters. Proper selection of FTIR operating parameters is important in photoacoustic measurements in order to optimize the signal-to-noise ratio and to control sampling depth as appropriate for a given investigation. Table 3.3 summarizes the parameter considerations to be made which are of particular importance in photoacoustic measurements.

Table 3.3 FTIR parameter selection considerations for photoacoustic measurements.

Parameter	Considerations
Resolution	When resolution is reduced by a given factor, signal-to-noise is improved by the square root of that factor for the same measurement time. Consequently, if an analysis can be done at 16 cm^{-1} or 32 cm^{-1} resolution rather than at 8 cm^{-1} resolution, analysis time can be reduced significantly. Resolution higher than 8 cm^{-1} is rarely needed for analysis of solids.
Number of Scans	Increasing the number of scans by a given factor increases signal-to-noise by the square root of that factor. 32 scans at 8 cm^{-1} resolution and a mirror velocity of 2.5 kHz (0.16 cm/s) is typical for survey work.
Continuous Scan Mirror Velocity	In studies where samples are homogenous and variable sampling depth is not desired, a single velocity can be used. Signal-to-noise for a given spectrum acquisition time improves as mirror velocity is reduced but photoacoustic signal saturation at high absorbance also increases. Mirror velocities from 400 Hz (0.25 cm/s) to 5 kHz (0.31 cm/s) are typical for both qualitative and quantitative analyses in the mid infrared. In the near infrared absorption is lower and a typical scan velocity of 100 Hz (0.063 cm/s) is more suitable. See Table 3.4 for information on modulation frequency ranges for spectral regions from the far infrared to the ultraviolet.
Modulation Frequency	See Section 3.2.2.
Beam Splitter and Source	Beam splitters and sources are optimized for specific spectral regions and should be chosen accordingly to optimize performance.
Aperture	The widest aperture should be chosen that is compatible with a given spectral resolution in order to maximize the incident beam intensity. An open aperture can usually be used for 8 cm^{-1} resolution and lower (16 cm^{-1}, 32 cm^{-1}, etc.).

3.2.2 Modulation Frequency A more comprehensive discussion of modulation frequency than could be accommodated in Table 3.3 is necessary due to its importance in varying the sampling depth of photoacoustic measurements.

FTIR spectrometers modulate the intensity of their light beam via changes in the optical path difference of the interferometer. Continuous motion of one of the interferometer

mirrors at constant velocity has been the traditional method of beam modulation in commercial instruments. More advanced FTIR spectrometers allow selection of either continuous motion or step-scan operation. Step-scan operation can be used to simulate low velocity continuous motion or in conjunction with phase modulation of the infrared beam intensity.

In the step-scan mode the optical path difference of the interferometer is changed in a series of incremental steps until a suitable interferometer path difference has been generated appropriate for the desired spectral resolution. The stepping motion can be achieved either by moving one interferometer mirror in steps while the other remains stationary or by oscillating one mirror with a saw tooth waveform while moving the other mirror at a constant velocity. This second method avoids the difficulty of bringing the stepping mirror to a dead stop and having to wait for transient mechanical vibrations to dampen out.

Phase modulation of the infrared beam intensity involves oscillating one of the mirrors about the step locations with an amplitude selected that corresponds to some number of helium-neon laser wavelengths. The phase modulation frequency must be well above the stepping frequency. The phase modulation frequency determines the sampling depth of the measurement and is constant across the whole spectrum being measured, in contrast to the variable sampling depth across the spectrum produced by continuous constant-velocity mirror motion.

If the phase modulation motion of the interferometer follows a square waveform, an AC signal can be measured which is generated by the beam intensity difference at the two extremes of the mirror oscillation. The infrared beam modulation frequencies generated by the square waveform are the fundamental frequency and the higher odd harmonics. Digital signal processing (DSP) allows simultaneous detection of orthogonal components of signals at the fundamental and odd harmonics. Data sets thus acquired allow infrared absorptions occurring in different sampling depth ranges to be studied on samples containing layers or concentration gradients.

3.2.2.1 Continuous Scan Mode Modulation. In the continuous scan mode the modulation frequency, f, is given by $f = \nu v$ where ν is the wavenumber location in the spectrum and v is the optical path difference (OPD) velocity. The OPD velocity is commonly given in units of cm/s but may also be given as the modulation frequency of the helium-neon laser beam, f_l, at a wavelength of 0.6328 μm (15,800 cm^{-1}). The expression $f = \nu f_l$ /15800 cm^{-1} gives the modulation frequency, f, at a given wavenumber, ν, corresponding to a velocity that generates a helium neon laser frequency of f_l.

Table 3.4 summarizes the interferometer generated modulation frequencies as a function of mirror velocity at the wavenumber limits of spectral regions including the far-infrared, mid-infrared, near-infrared, and visible-ultraviolet. Frequencies above 16 kHz and below 1 Hz are not included in the table because they are beyond the frequency range for which

the detector has good sensitivity operating with a helium gas atmosphere. Selection of a mirror velocity within the available ranges depends on the sampling depth, L, required, which is given by the expression $L = (D/\pi f)^{1/2}$. Sampling depths are plotted in Figure 2.5 for different mirror velocities. The expression can also be written as $L = (D/\pi v v)^{1/2}$ or $L = (\nu_\ell D/\pi v f_\ell)^{1/2}$ where ν_ℓ = 15,800 cm^{-1}. In measurements on polymers a value of 1 x 10^{-3} cm^2/s is often used for D since the thermal diffusivity of many common polymers are approximately equal to this value.

Table 3.4 FTIR modulation frequencies generated by different OPD velocities

OPD Velocity		far IR	mid IR	near IR	visible-UV	
cm/s	Hz	50cm^{-1}	400cm^{-1}	4000cm^{-1}	10000 cm^{-1}	50000 cm^{-1}
.003	5			1.26Hz	3.15Hz	15.8Hz
.006	10			2.53	6.30	31.6
.016	25			6.32	15.8	79.1
.063	100		2.53Hz	25.3	63.2	316
.025	400	1.27Hz	10.1	101	253	1260
0.05	800	2.53	20.2	202	504	2530
0.16	2.5k	7.91	63.2	632	1580	7910
0.31	5k	15.8	127	1260	3150	15800
0.63	10k	31.6	253	2530	6300	
1.25	20k	63.2	506	5060	12600	
2.5	40k	127	1010	10100		
5.00	80k	253	2020			
7.50	120k	381	3030			

3.2.2.2 Phase Modulation Mode Phase modulation is used exclusively with step scanning. In phase modulation, one mirror oscillates at a selected frequency and amplitude about each step position. The signal from the photoacoustic detector is then processed by a phase-sensitive detector locked to the phase-modulation frequency to measure the two orthogonal components (in-phase and quadrature) of the signal, ultimately resulting in two interferograms. Both signal magnitude and phase can then be derived from these components. It is the phase-modulation frequency, not the spectrometer scanning speed, that controls the sampling depth and the depth resolution provided by phase, as illustrated in Figure 2.5 and Table 2.1, respectively. If the phase-modulation oscillation produced by a spectrometer is not a sine wave (typically, it is a square wave), then digital signal processing (DSP) can be substituted for a phase-sensitive detector to make measurements simultaneously at the fundamental phase-modulation frequency and certain of its harmonics.

The amplitude of the phase-modulation oscillation affects how efficiently (or how completely) the spectrometer light beam is modulated [10]. Whenever the peak-to-peak

amplitude of the oscillation equals the wavelength of the light or an integer multiple of it, the light is not modulated at all because the amount of interference produced by the interferometer is the same at the two extremes of the oscillation. Conversely, whenever the oscillation amplitude is equal to half the wavelength or an odd multiple of it, the modulation is maximized. Spectrometers are commonly set up so that the available peak-to-peak amplitudes of the phase-modulation oscillation are integer multiples of half the helium-neon laser wavelength. In that case, the wavenumber positions of the modulation nodes, ν_p^{min} and maxima, ν_p^{max}, are given by:

$$\nu_p^{max} = (p - 1/2)\nu_{HeNe}/n \qquad (3.1)$$

and

$$\nu_p^{min} = p\nu_{HeNe}/n \qquad (3.2)$$

where ν_{HeNe} is the helium-neon laser wavenumber (15800 cm^{-1}), n is the peak-to-peak amplitude of the oscillation measured in helium-neon laser wavelengths (n= .5, 1, 1.5, ...), and p is an index (p = 1, 2, 3, ...). The first few nodes and maxima for selected values of n are given in Table 3.5. At present, most spectrometers provide amplitudes only up to about n = 2. No photoacoustic signal is produced at the modulation nodes and the highest instrumental signal-to-noise ratios occur at the modulation maxima. The phase-modulation amplitude should therefore be chosen to place all nodes outside the spectral range of interest, and, when possible, a modulation maximum near the region of interest.

Table 3.5 Interferometric wavenumber maxima and minima for different phase modulation amplitudes given in HeNe laser wavelengths, *n*.

n	$\nu_1^{max}(cm^{-1})$	$\nu_1^{min}(cm^{-1})$	$\nu_2^{max}(cm^{-1})$	$\nu_2^{min}(cm^{-1})$	$\nu_3^{max}(cm^{-1})$	$\nu_3^{min}(cm^{-1})$	$\nu_4^{max}(cm^{-1})$
.25	31610	63210					
.5	15803	31606	47408	63211			
1.0	7901	15803	23704	31606	39507	47408	55310
1.5	5268	10535	15803	21070	26338	31606	36873
2.0	3950	7901	11852	15803	19753	23704	27655
2.5	3161	6321	9482	12642	15803	18963	22124
3.0	2634	5268	7901	10535	13169	15803	18437
5.0	1580	3161	4741	6321	7901	9482	11062
10.0	790	1580	2370	3161	3951	4741	5531
20.0	395	790	1185	1580	1975	2370	2766

The higher n values given in Table 3.5 are not presently available on most step-scan spectrometers but were included to show how the extrema would vary with amplitude if such amplitudes are available. Selection of available n values on a particular spectrometer

for the spectral region desired should be based primarily on the ν_1^{max} and ν_1^{min} values in Table 3.5, but the overall system response curve should be checked with the carbon black reference in the photoacoustic detector prior to running sample spectra since it is sensitive to the other spectral variations of the source and optics.

3.2.3 Data Handling. Photoacoustic FTIR interferograms are transformed by the standard FTIR data system algorithms used with other sampling techniques and detectors. The resulting photoacoustic spectra are absorbance spectra and are normalized by dividing the sample spectrum by a background spectrum obtained with a carbon black or other reference sample. The ordinate label may be given as photoacoustic, absorbance, or transmittance units depending on the FTIR. Depending on how the particular FTIR software is set up, it may be necessary to change the label to absorbance, if it is not already so, in order to do qualitative or quantitative analyses. It is important to note that photoacoustic absorbance units are sensitive to amplifier gain settings, sample condition (slab versus powder), and the gas atmosphere and volume of the detector.

Qualitative analysis can be done with photoacoustic FTIR spectra using commercial and user-generated libraries. Libraries in the former case are often based on transmission measurements resulting in differences between ordinate values of library and photoacoustic spectra due to arbitrary PAS units and to different effective sampling thicknesses and consequent signal saturation variations. This situation is not unique to photoacoustic sampling since many transmission and reflectance based unknown spectra do not perfectly match commercial library spectra on the ordinate axis. Photoacoustic spectra show good coincidence on the wavenumber axis with commercial libraries.

User-generated photoacoustic spectral libraries produce good coincidence on the ordinate axis, provided that amplifier gain is set consistently at the same levels for sample and background spectrum acquisitions and that the sample condition is consistent. If condition varies, for instance, from a slab to a powder, the signal level will shift upward, but this does not significantly influence qualitative analyses. Coincidence between photoacoustic library and unknown spectra is excellent on the wavenumber axis.

Standard FTIR factor analysis software packages for quantitative analysis work well with photoacoustic spectra, typically producing standard errors of prediction of less than 1%. Both PLS and PCR tolerate the nonlinearities (due to signal saturation) present in photoacoustic spectra well. Quantitation using a single band is also possible with FTIR-PAS spectra. Both approaches are demonstrated in Section 4.

4.0 Applications

4.1 Introduction

Applications discussed in this section were chosen from work in the authors' laboratory to illustrate important capabilities of PAS including rapid qualitative analysis, quantitative analysis, and variation of sampling depth to reveal depth varying composition. Readers are referred to the general scientific literature for a wider scope of applications [2, 11, 12, 13, 14, 15, 16].

4.2 Rapid Identification of Polymers for Recycling

Recycling of polymers is expanding due to both environmental and economic factors. There are two main classes of polymers. These are the less valuable consumer polymers used, for instance, in plastic household containers and the more costly and more difficult to analyze engineering polymers used in motor vehicles, computers, and appliances. The value of recycled engineering polymers is increased if the material can be accurately sorted as to both general polymer type and subtype, which is related to filler and additive concentrations.

Polymer recycle operations require fast and modestly priced equipment given the economics involved. Hence, a low priced FTIR (Perkin-Elmer Paragon 1000) was used in this study [17] with an MTEC model 300 photoacoustic detector. Samples were punched (0.285 diameter) from typical polymer car components supplied by Ford and MBA Polymers Inc. Punching time was approximately 2 s/sample. Samples were positioned in a special sample holder so that the infrared beam impinged on the cut cross-section, thus avoiding the need to remove surface coatings that are present on many car components. FTIR-PAS spectra (3000 cm^{-1} - 500 cm^{-1}) were acquired in one scan (0.1 cm/s OPD velocity, 16 cm^{-1} resolution, helium-purge) and identified using the Perkin-Elmer "Compare" function in a total of 5 sec. Minor modifications were made on the Paragon to increase the speed of data acquisition and analysis.

A library of 19 spectra were used to identify 35 "unknowns" as to general polymer type (xenoy, polyurethane, ABS, and polypropylene) and as to talc filler level in polypropylene. The identification accuracy was 100% for both general polymer type and talc filler level [17].

4.3 Quantitative Analysis of Major and Minor Concentrations of Additives in Paper Products

Most paper products contain surface and bulk additives at different concentrations to produce various special properties. Figure 4.1 shows FTIR-PAS spectra of paper towels with varying concentrations of latex to produce wet strength. The spectra were measured at 8 cm^{-1} resolution, 128 scans, at a mirror velocity of 2.5 kHz laser fringe frequency. Magnesium perchlorate desiccant was used in the sample cup. The samples were predried overnight at 110°C in air. The starred cellulose band was used to scale the ordinate axis of the spectra. The latex constitutes a major bulk additive in the paper ranging from 12.3% to 29.8% by weight.

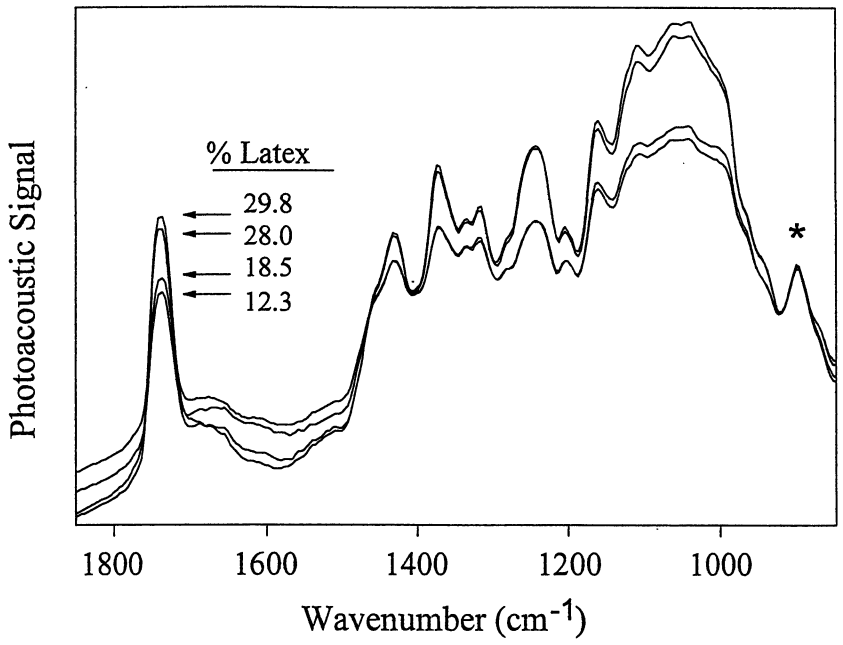

Figure 4.1 FTIR-PAS spectra of paper towels with different concentrations of latex. The spectra are normalized to the starred cellulose band.

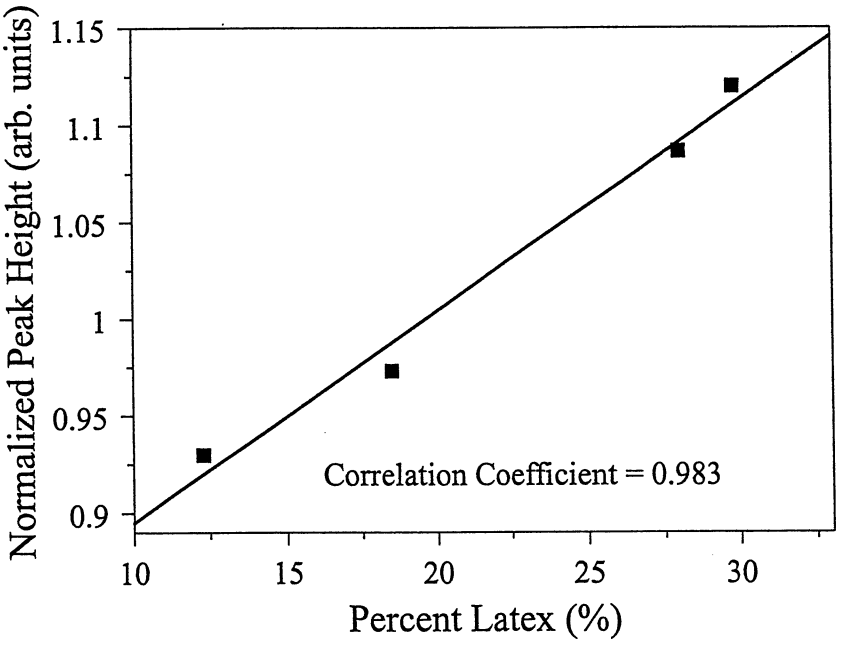

Figure 4.2 Correlation plot for the latex in paper analysis.

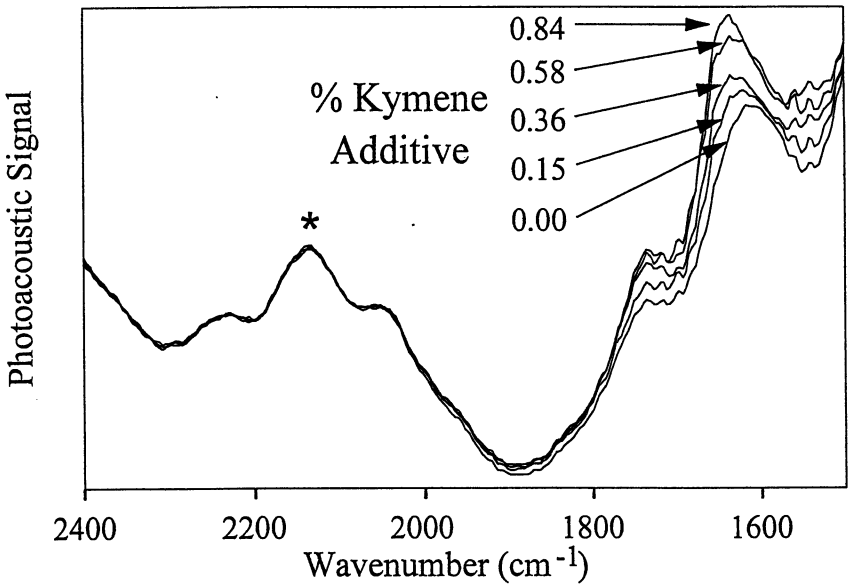

Figure 4.3 FTIR-PAS spectra of Kymene in paper. The spectra are normalized to the starred cellulose band.

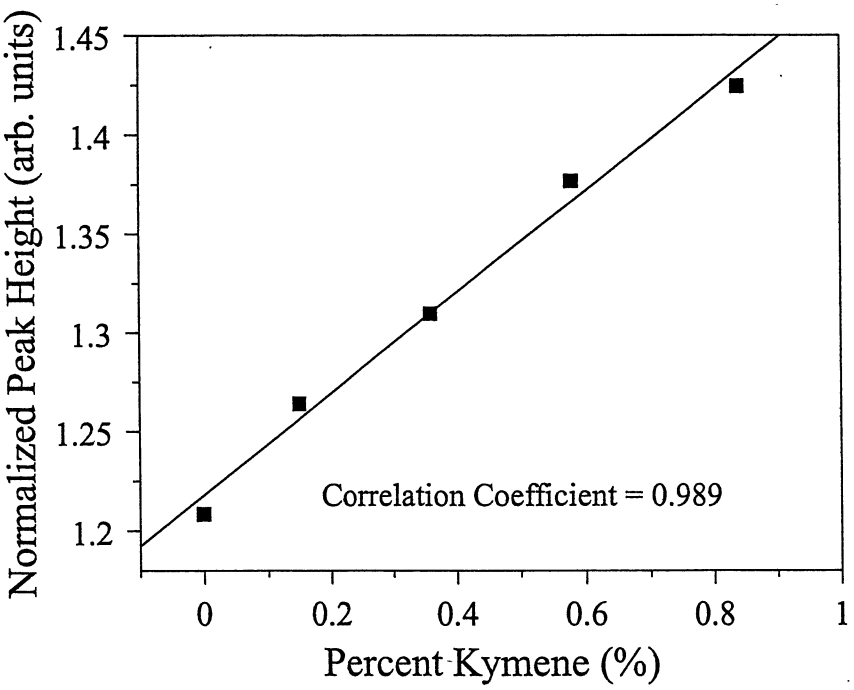

Figure 4.4 Correlation plot for the Kymene in paper analysis.

Figure 4.2 shows the scaled peak height of the latex band at 1735 cm^{-1} as a function of latex concentration. The latex peak heights were measured relative to the baseline which varies significantly for these samples. A correlation coefficient of 0.983 was calculated for this analysis.

Analysis of minor concentrations of additives in paper is also possible with FTIR-PAS. Paper spectra with a kymene bulk additive (concentration range 0.0% to 0.84% by weight) are shown in Figure 4.3. The starred paper band at 2140 cm^{-1} was used to scale the spectra. Measurement and drying conditions were the same as for the latex analysis. Figure 4.4 shows the correlation between the kymene concentration and normalized kymene peak height near 1600 cm^{-1}. A correlation coefficient of 0.989 was calculated for this analysis. Factor analysis was not used in either paper analysis because of the limited number of samples.

4.4 Analysis of Aqueous Sludges with Soluble and Insoluble Species

Analysis of nuclear waste tank sludges is important in waste clean-up operations. FTIR-PAS is an ideal molecular analysis method because it allows small amounts of radioactive material to be analyzed with minimal handling and radiation exposure [18]. In this application, approximately 1 mg samples of non-radioactive surrogate were analyzed. The samples contained both soluble and insoluble salts in an aqueous sludge. Soluble salts in the moist sludge tended to be partly in solution and partly crystalized, leading to variability in the infrared spectra as the moisture level varied. Therefore, the samples were dried to obtain reproducible spectra. The drying procedure is critical for this type of sample because conventional air or oven drying causes the soluble components to migrate to the sample surface and form macrocrystals. This inhomogeneous condition results in an increase of soluble species' peak heights and spectral distortion from crystal refraction effects. Freeze drying, on the other hand, produces microcrystals with no migration of soluble species because they are initially frozen in place and water is removed by sublimation.

Figure 4.5 shows spectra of a surrogate sludge dried by the different methods. The presence of macrocrystal formation is especially apparent in the air dried spectrum where the soluble nitrate band intensities (1798 cm^{-1} and 2433 cm^{-1}) are increased relative to the insoluble ferrocyanide band (2098 cm^{-1}). Figure 4.6 shows the phase behavior of the sodium nitrate band at 1789 cm^{-1} and of the ferrocyanide band at 2098 cm^{-1} for samples dried by the different methods. The strong ferrocyanide band's phase leads that of the weaker nitrate band as would be expected. The phase in the case of ferrocyanide is the same for all drying methods because there is no migration to the surface of insoluble species. On the other hand, the nitrate phase for air and oven dried samples leads that of the freeze dried indicating migration of soluble species to the surface for air and oven dried samples.

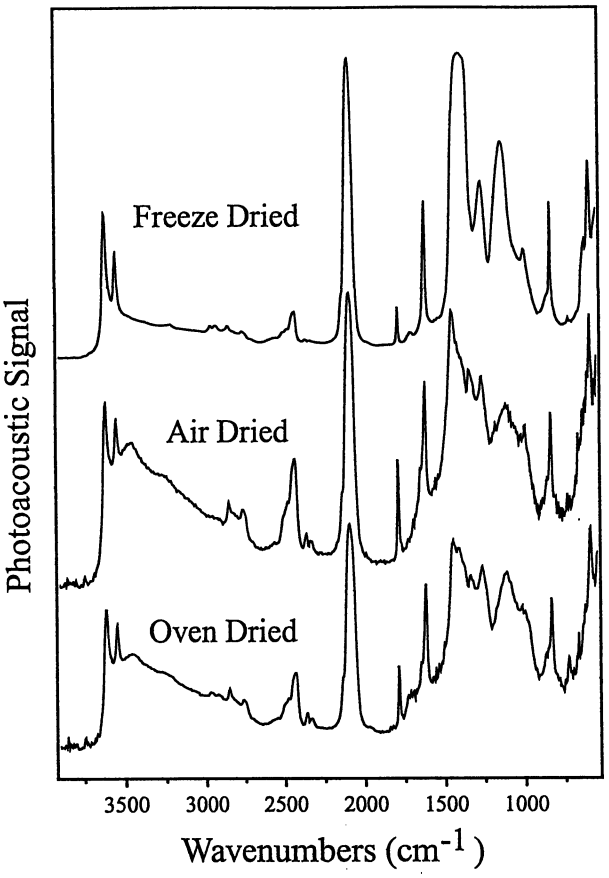

Figure 4.5 FTIR-PAS spectra of a surrogate nuclear waste tank sludge which was dried by three different methods as indicated. Reproduced from [8].

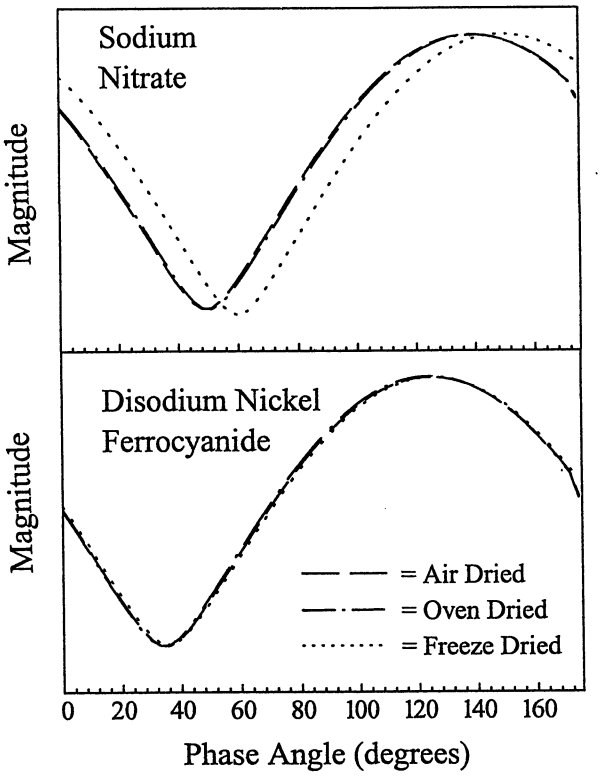

Figure 4.6 Phase angle behavior for soluble sodium nitrate species and insoluble disodium nickel ferrocyanide species after drying by different methods. The phase zero is arbitrary. Reproduced from [8].

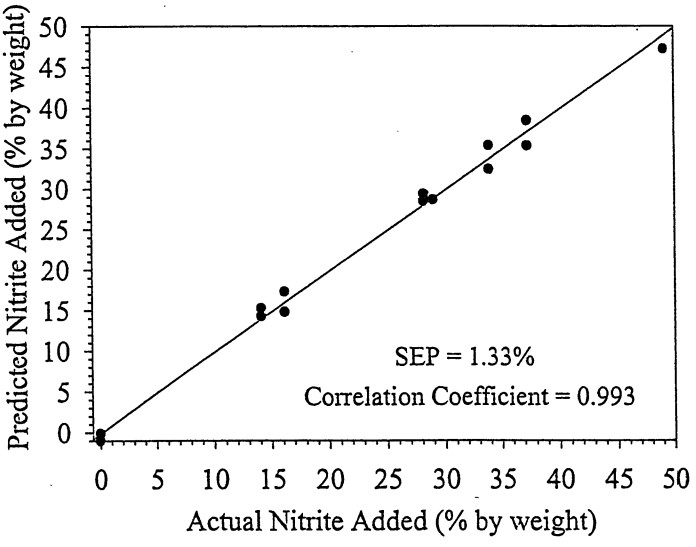

Figure 4.7 Correlation plot for sodium nitrite in sludge analysis.

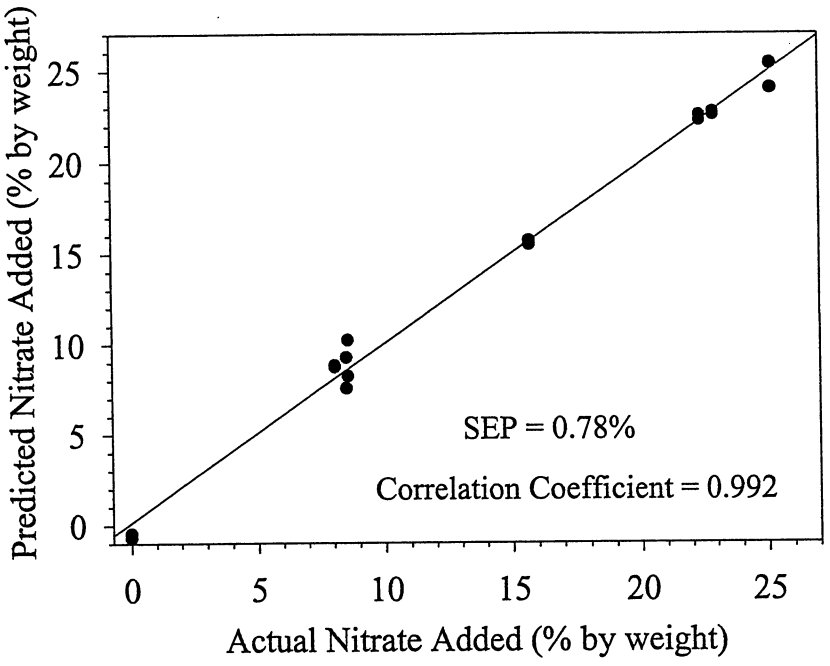

Figure 4.8 Correlation plot for sodium nitrate in sludge analysis.

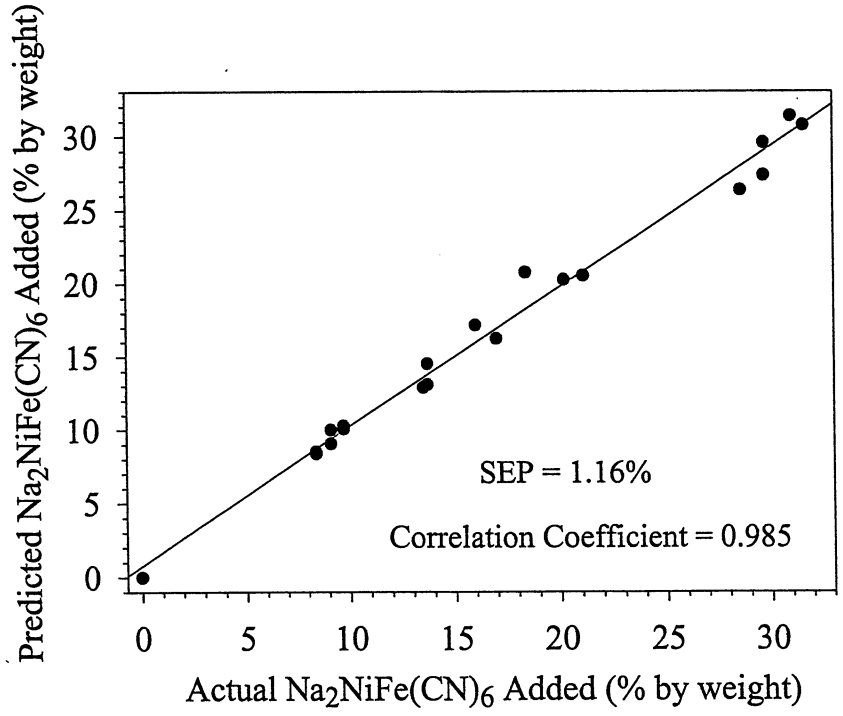

Figure 4.9 Correlation plot for disodium nickel ferrocyanide in sludge analysis. Adapted from [8].

Figures 4.7, 4.8, and 4.9 are plots for nitrite, nitrate, and disodium nickel ferrocyanide, respectively, showing the correlations between the concentrations predicted from FTIR-PAS spectra by a PLS routine and the concentrations known from synthesis. Samples were prepared by adding known amounts of a single salt species to surrogate sludge

supplied by the Westinghouse Hanford Company and then freeze drying the sample for six hours at -50°C using a Fisons Model 350 freeze dryer. Spectra were measured at 8 cm^{-1} resolution with 256 scans and a mirror velocity of 2.5 kHz. The standard errors of prediction (SEP) and correlation coefficients suffer to some degree from mixing difficulties during synthesis of these types of samples.

4.5 Quantitation of $CaCO_3$ Residual in Lime

Lime (CaO) is produced by heating limestone ($CaCO_3$) in a kiln. It is desirable to calcine as much $CaCO_3$ as possible into CaO without exposing the CaO to too much heating, which reduces its reactivity. Processing is considered optimal if the residual $CaCO_3$ concentration is approximately 1%.

Figure 4.10 shows FTIR-PAS spectra of lime containing various concentrations of $CaCO_3$ (0-5%) measured at 8 cm^{-1} resolution, 2.5 kHz mirror velocity, and 256 scans. The spectra were normalized against an adjacent CaO band to remove scaling variations due to particle size or packing. The samples were synthesized in powder form from reagent grade $CaCO_3$ and CaO and were placed in stainless steel inner cups for analysis. They were dried overnight in a desiccator to remove moisture. This step would probably not be necessary for samples coming directly out of a kiln.

The plot in Figure 4.11 gives the correlation between the $CaCO_3$ peak at 2513 cm^{-1} and the limestone concentration which is known from synthesis of the samples. The correlation coefficient for the analysis is 0.997%.

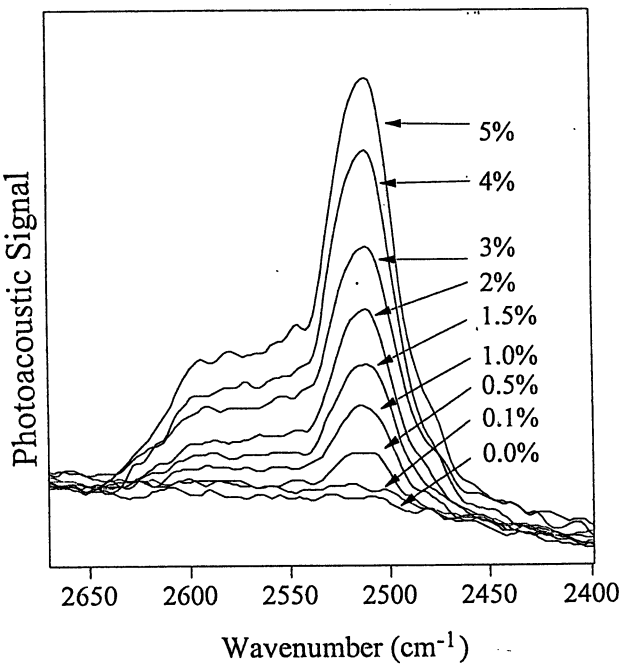

Figure 4.10 FTIR-PAS spectra of lime with different concentrations of uncalcined $CaCO_3$.

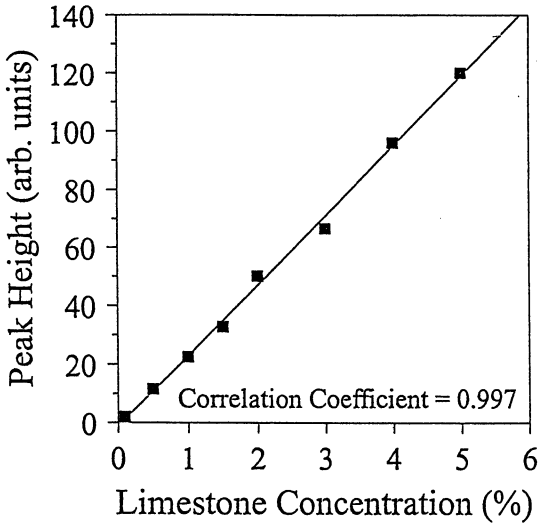

Figure 4.11 Correlation plot of $CaCO_3$ in lime.

4.6 Determining Surface or Bulk Character of Polymer Additives

Polymer additives are often specialized to concentrate at the surface or be homogeneously distributed in the bulk. Figure 4.12 shows FTIR-PAS spectra of polyethylene containing both surface (1645 cm^{-1}) and bulk (1019 cm^{-1}) additive bands measured at mirror velocities of 200 Hz (20 scans), 2.5 kHz (200 scans), and 20 kHz (10,000 scans) corresponding to sampling depths of approximately 50 μm, 10 μm and 4 μm, respectively. The spectra have been scaled so that the polyethylene peak marked N is of constant height. Note that the surface additive peak height grows substantially as sampling depth is reduced indicating a surface or near surface additive concentration whereas the bulk additive peak increases much more gradually due to reduction in signal saturation with increasing frequency. The strong off scale polyethylene peak heights also increase due to reduced photoacoustic signal saturation at higher frequency as discussed in Section 2.4.

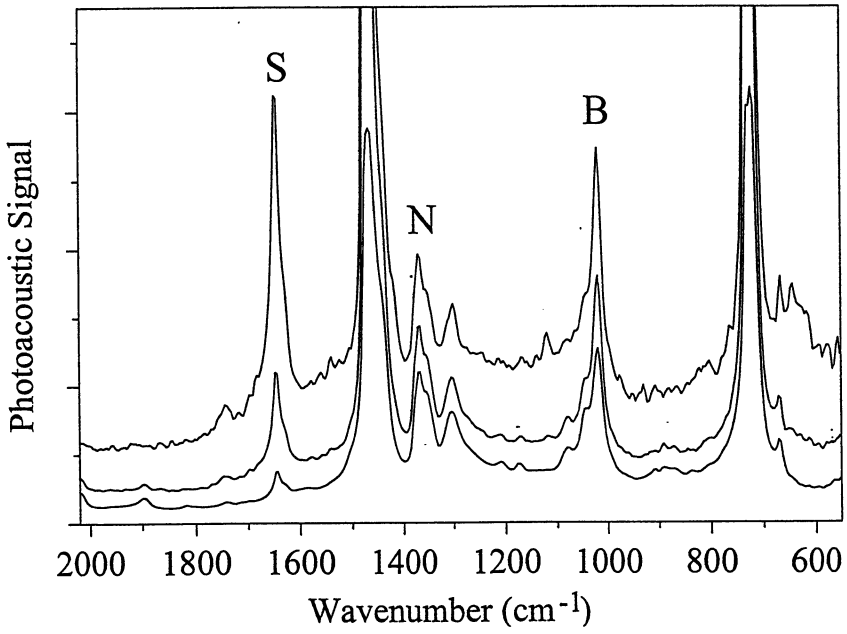

Figure 4.12 FTIR-PAS spectra of polyethylene pellets with bands associated with a surface (S) segregating additive and a bulk (B) additive. The spectra were measured at mirror velocities of 200 Hz (lower), 2.5 kHz (middle), and 20 kHz (top) and are normalized to the band labeled N. The approximate sampling depths (top to bottom) are 4 μm, 10 μm, and 50 μm.

The phase behavior of the surface bulk, and the strongest polyethylene (2920 cm^{-1}) bands are plotted in Figure 4.13. Figure 4.14 shows a magnitude spectrum of the polyethylene sample. The data in Figures 4.13 and 4.14 were measured using a phase modulation optical path difference amplitude of 2 helium-neon laser wavelengths, 400 Hz modulation frequency, 8 cm^{-1} resolution, and 16 scans. The in-phase and quadrature photoacoustic signal were measured simultaneously and the plots were calculated from these components.

The magnitude of the surface additive band (S) is smaller than that of the bulk additive band (B) in Figure 4.14 but the phase of the additive band (120°) is seen to lead that of the bulk band (147°). This magnitude and phase behavior indicates that the 1645 cm^{-1} band (S) is definitely associated with a surface segregating additive. The phase data also allows determination as to if the additive consists of a layer on the surface or is localized near the surface. The fact that the phase of the strong polyethylene band at 2920 cm^{-1} leads the additive band in phase indicates that the additive is not a surface layer on top of the polyethylene but must extend to some degree below the polymer surface.

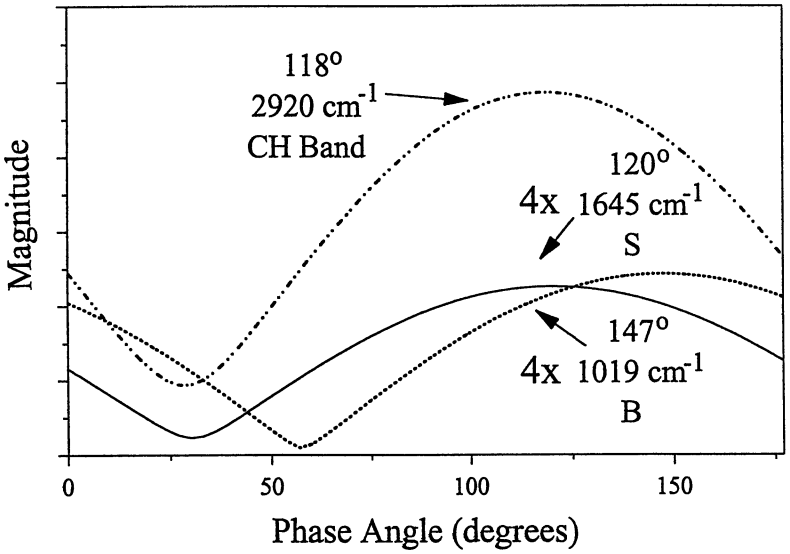

Figure 4.13 Phase-modulation phase behavior of the surface additive band (S), bulk additive band (B), and the strong C-H polyethylene band. The phase zero is arbitrary.

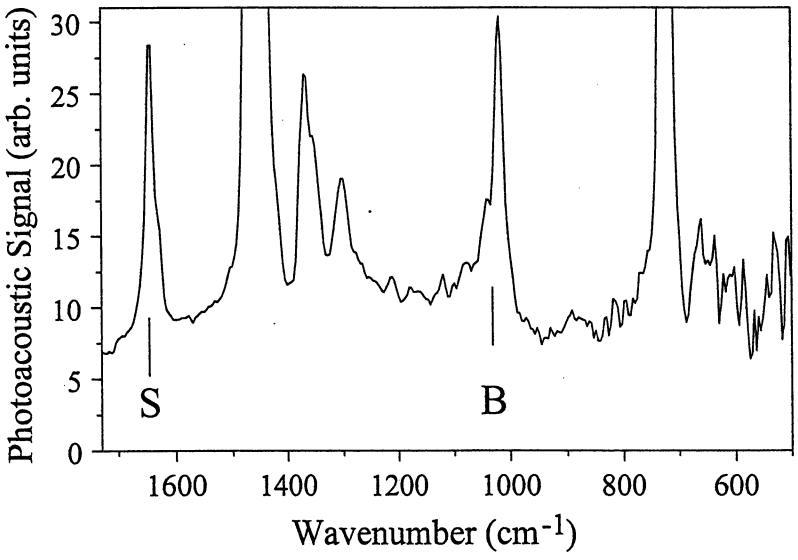

Figure 4.14 FTIR-PAS magnitude spectrum calculated from the same data set used for Figure 4.13. The data were measured by 400 Hz phase modulation.

4.7 Fluorination of Polyethylene

Polyethylene containers and motor vehicle gas tanks are fluorinated to produce a surface layer that reduces fluid permeability. It is important to be able to measure the level of fluorination in order to achieve economical processing and to establish quality control standards. FTIR-PAS provides a method to satisfy both these production needs and to provide depth information to assist in process development.

In Figure 4.15, phase modulation FTIR-PAS magnitude spectra are plotted for polyethylene with high and low levels of fluorination, as indicated by the broad band at 1100 cm^{-1}. Figure 4.16 shows the phase behavior of the fluorination band at high and low levels, the strongest polyethylene band at 2920 cm^{-1}, and the next strongest at 1470 cm^{-1}. The phases of the high and low level fluorination band lead the phase of the strong polyethylene C-H band at 2920 cm^{-1} indicating that the main fluorination region is within a few micrometers of the surface.

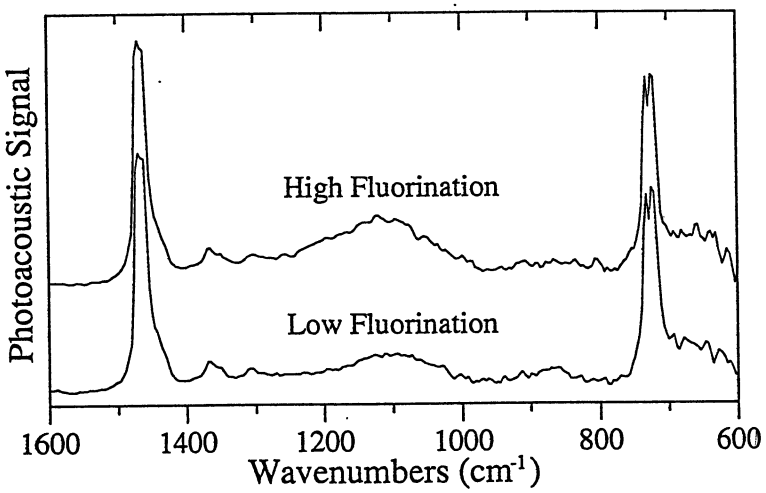

Figure 4.15 Phase-modulation FTIR-PAS spectra of polyethylene with high and low levels of fluorination.

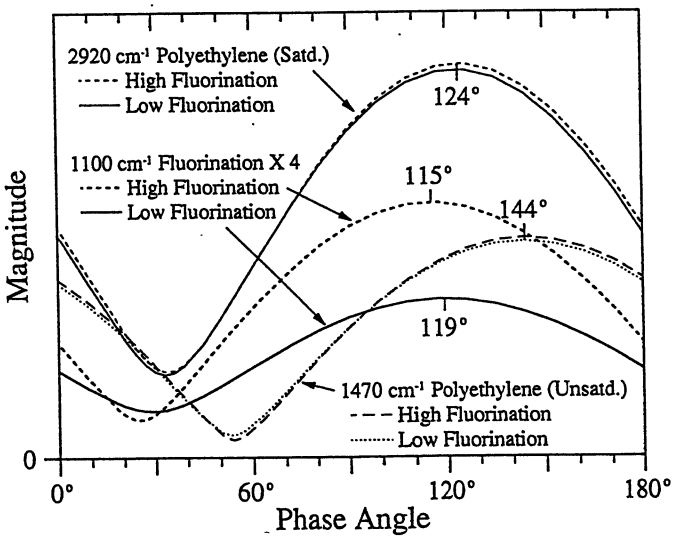

Figure 4.16 Phase behavior for fluorination and polyethylene bands. The phase zero is arbitrary.

4.8 Chemical Surface Treatment of Polystyrene Spheres

This application illustrates the use of phase information to indicate the layering order of a sample. Figure 4.17 shows the FTIR-PAS spectrum of polystyrene spheres which have a surface layer due to chemical treatment. The marked bands are associated with hydroxyl (OH), surface treatment (surface), and strong (SB) and weak (WB) bands of the polystyrene matrix. The phase behavior of these bands is also shown in Figure 4.17. The hydroxyl and surface treatment bands are much weaker than the strong polystyrene band, but they still lead it in phase. The hydroxyl species must be on the surface of the chemical treatment species, because the hydroxyl band has the smallest phase shift and has approximately the same peak magnitude as that of the chemical treatment species.

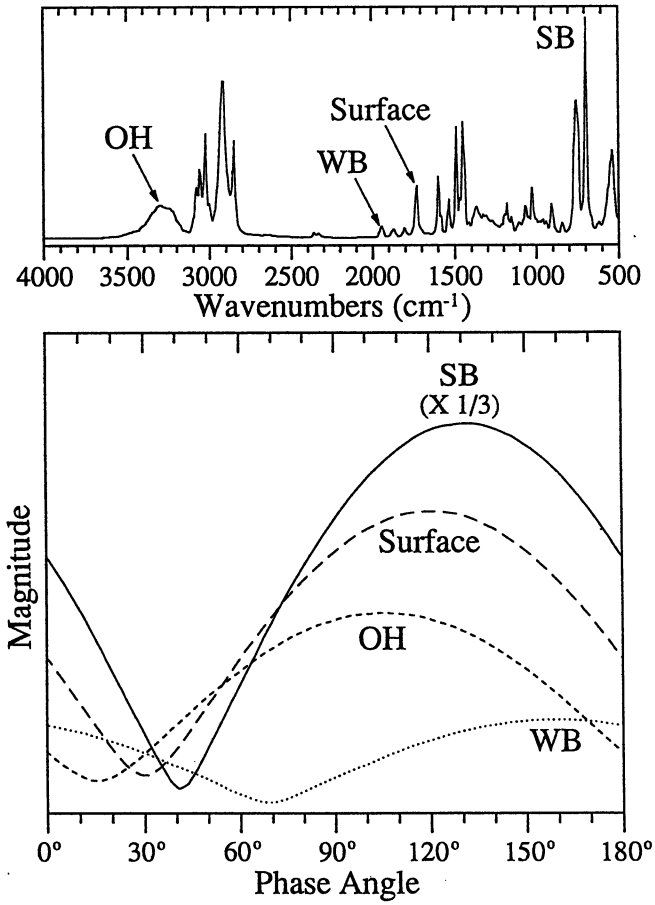

Figure 4.17 Phase-modulation FTIR-PAS spectrum and phase behavior for polystyrene spheres with chemically treated surfaces. The phase zero is arbitrary.

4.9 Enhanced Surface Specificity by Linearization of FTIR-PAS Spectra

In Section 2.5, FTIR-PAS spectrum linearization using Equation 2.3 is discussed as a method to decrease sampling depth beyond the limit imposed by the maximum modulation frequency that is practical for measurements [7]. Figure 4.18 shows the usual magnitude spectra (5 kHz and 40 kHz) and the linearized spectrum (40 kHz) of a paper with a polyethylene inner coating and thin silicone outer coating. Note the growth with reduced

sampling depth of the silicone bands (1261 cm^{-1}, 1022 cm^{-1}, and 798 cm^{-1}) relative to the polyethylene band at 1466 cm^{-1}. The sampling depths near 1000 cm^{-1} for the 5 kHz, 40 kHz, and 40 kHz-linearized spectra are 10 μm, 3 μm, and 1 μm. At these depths none of the paper bands are observed.

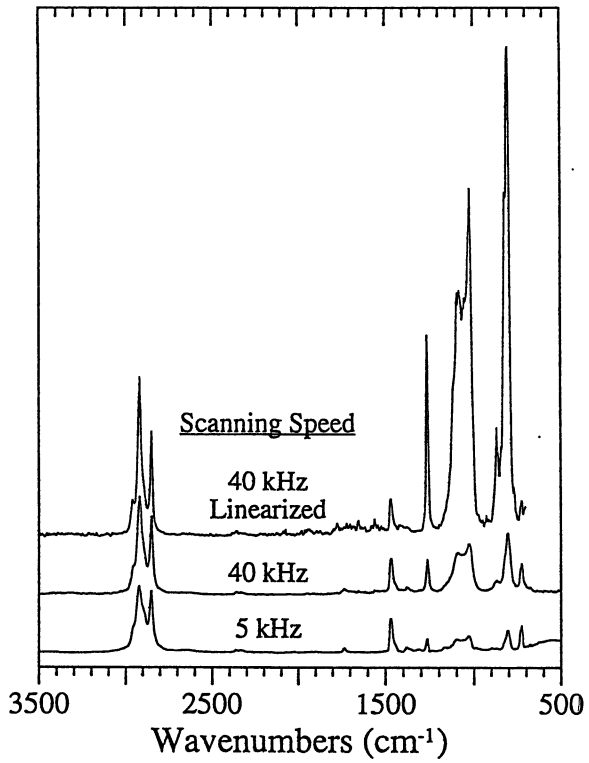

Figure 4.18 Variable sampling depth FTIR-PAS spectra of a silicone-on-polyethylene coated paper. Spectra have been scaled to the 1466 cm^{-1} band.

4.10 Determination of Coating Thickness from Phase Data

In this application, a calibration curve is produced for predicting the thickness of PET films on polycarbonate [9] based on Equation 2.10. FTIR-PAS spectra are measured for 5 PET coating thicknesses (2.5, 3.6, 6.0, 12, and 23 μm), for the bare polycarbonate substrate, and for a thick specimen of PET. The latter measurement is needed to correct for the small absorption of the infrared beam by the thicker PET films at the 1778 cm^{-1} polycarbonate band, the band which is used for the phase versus coating thickness measurements [9]. Figure 4.19 shows the phase behavior for the 1730 cm^{-1} PET band and the 1778 cm^{-1} polycarbonate band that results for different coating thicknesses. The calibration curve is plotted in Figure 4.20 using the phase data of Figure 4.19. The solid circles are the phases observed in Figure 4.19. The solid line is calculated from Equation 2.10 using $L = 8.9$ μm and plotted with an abscissa intercept of 132°. The first four points fit the calculation but the 12 and 23 μm points deviate substantially due to overlap by the wing of the 1730 cm^{-1} PET band. The absorption in the thick PET films contributes a fast signal component resulting in measurement of smaller phase angle values than would

occur if the film were completely transparent. The measured phase values can be corrected using Equations 2.11 and 2.12 [9]. The corrected points are shown as open circles in Figure 4.20.

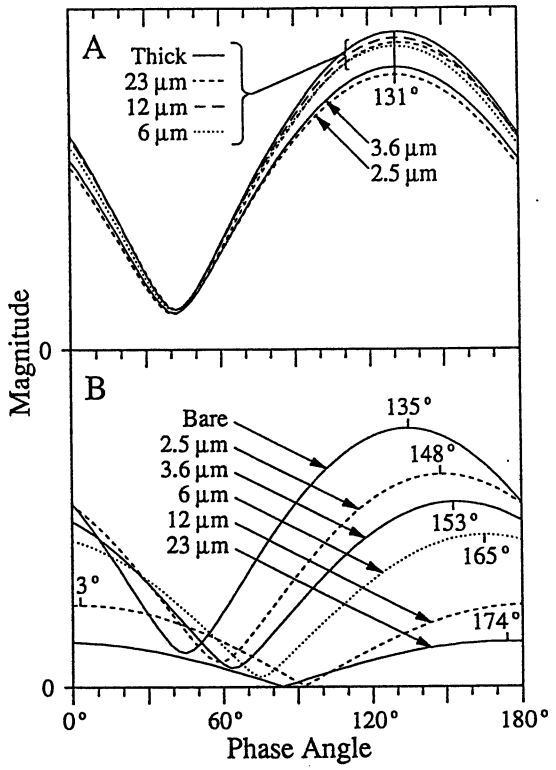

Figure 4.19 Phase behavior for a PET coating band peak (A) and for a polycarbonate band peak (B) measured for samples having the indicated thickness of PET coated onto thick polycarbonate, as well as for "Bare" polycarbonate and a "Thick" piece of PET. The phase zero is arbitrary. Reproduced from [9].

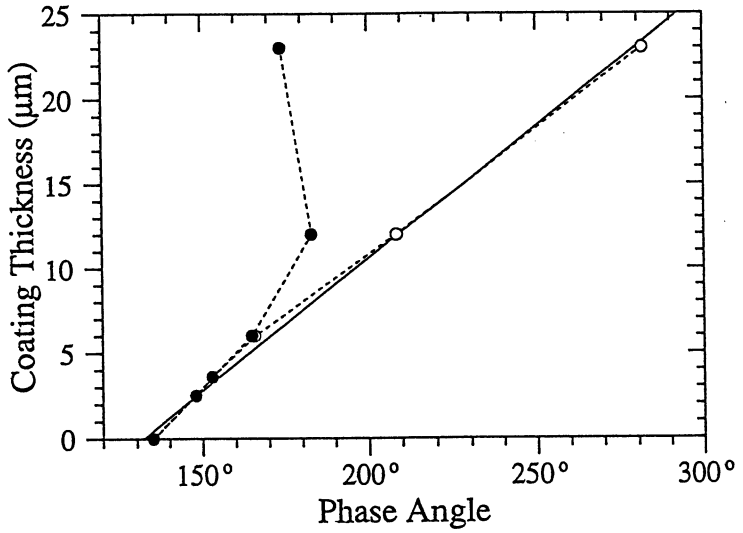

Figure 4.20 Calibration curve relating the PET coating thickness to phase angle. The open circles represent corrected phase values. Reproduced from [9].

5.0 Conclusion

As stated in the introduction, this chapter discusses advances in FTIR-PAS in the last four years since publication of "A Practical Guide to FTIR Photoacoustic Spectroscopy" [2]. Most significant are the reduction in FTIR-PAS analysis time to 5 s/sample discussed in Section 4.2 and variable-depth probing using both magnitude and phase data. This latter area of advancement is closely tied to step-scan interferometry with phase modulation.

FTIR-PAS is expected to continue to grow in use at both ends of user sophistication. At the low end, users will continue to be attracted by the ease of dropping a sample in the cup and getting a spectrum for qualitative analysis. At the high end, researchers will develop more advanced variable depth analysis capabilities. Between these two user extremes, continued development and use of the quantitative analysis capabilities of FTIR-PAS is expected to occur.

6.0 Acknowledgements

This work was funded by MTEC Photoacoustics, Inc. and the U.S. Department of Energy, Office of Science and Technology. Ames Laboratory is operated for the U.S. Department of Energy by Iowa State University under Contract No. W-7405-ENG-82.

The authors wish to thank the Digilab Division of Bio-Rad for the loan of an FTS 60A FTIR spectrometer used in some of the work and for technical support. Samples for application studies were supplied by Glenn Norton (Ames Laboratory), Richard Kellner (Technical University of Vienna), Teo Rebagay (Westinghouse Hanford Co.), Mike Biddle (MBA Polymers), and Patsy Coleman (Ford Motor Co.).

7.0 References

[1] A.G. Bell, *Phil. Mag.* 11, 510 (1881).

[2] J.F. McClelland, R.W. Jones, S. Luo and L.M. Seaverson, "A Practical Guide to FT-IR Photoacoustic Spectroscopy", in *Practical Sampling Techniques for Infrared Analysis*, P.B. Coleman, Ed. (CRC Press, Boca Raton, Florida, 1993), Chapter 5.

[3] A. Rosencwaig and A. Gersho, *J. Appl. Phys.* 47, 64 (1976).

[4] J.G. Parker, *Appl. Opt.* 12, 2974 (1973).

[5] F.A. McDonald and G.C. Wetsel, Jr., *J. Appl. Phys.* 49, 2313 (1978).

[6] A. Mandelis, Y.C. Teng and B.S.H. Royce, *J. Appl. Phys.* 50, 7138 (1979).

[7] R.O. Carter III, *Appl. Spectroscopy* 46, 219 (1992).

[8] H.S. Carslaw and J.C. Jaeger, *Conduction of Heat in Solids*, (Oxford, Clarendon, 1959).

[9] R.W. Jones and J.F. McClelland, *Appl. Spectroscopy*, 50, 1258 (1996).

[10] R.A. Crocombe, J.C. Leonardi and D.B. Johnson, "Signal Processing in Step-Scan FT-IR", in *Proc. 9th International Conference on Fourier Transform Spectroscopy*, SPIE Vol 2089 (SPIE, Bellingham, WA, 1994), 244.

[11] D.R. Bauer, M.C.P. Peck and R.O. Carter III, *J. Coatings Tech.* 59, 103 (1987).

[12] M-L. Kuo, J.F. McClelland, S. Luo, P-L. Chien, R.D. Walker and C-Y. Hse, *Wood Fib. Sci.* 20, 132 (1988).

[13] C.Q. Yang, *Appl. Spectroscopy* 45, 102 (1991).

[14] R.M. Dittmar, J.L. Chao and R.A. Palmer, *Appl. Spectroscopy* 45, 1104 (1991).

[15] S. Luo, C-Y. F. Huang, J.F. McClelland and D.J. Graves, *Anal. Biochem.* 216, 67 (1994).

[16] A.O. Salnick and W. Faubel, *Appl. Spectroscopy* 49, 1516 (1995).

[17] S.J. Bajic, J.F. McClelland, P. Coleman and M.M. Biddle, to be submitted to *Appl. Spectroscopy*

[18] S.J. Bajic, S. Luo, R.W. Jones and J.F. McClelland, *Appl. Spectroscopy* 49, 1000 (1995).

8.0 Index

Index (continued)